# Learning a Spatial Partitioning and its Causal Relations from Temporal Data

**Philippe Brouillard** BROUILPH@MILA.QUEBEC
*Université de Montréal | Mila - Quebec AI Institute*

**Sébastien Lachapelle** S.LACHAPELLE@SAMSUNG.COM
*Samsung AI Lab, Montreal*

**Julia Kaltenborn** JULIA.KALTENBORN@MILA.QUEBEC
*Mila - Quebec AI Institute | McGill University*

**Yaniv Gurwicz** YANIV.GURWICZ@INTEL.COM
*Intel Labs*

**Dhanya Sridhar** DHANYA.SRIDHAR@MILA.QUEBEC
*Université de Montréal | Mila - Quebec AI Institute*

**Alexandre Drouin** ALEXANDRE.DROUIN@SERVICENOW.COM
*ServiceNow Research | Mila - Quebec AI Institute*

**Peer Nowack** PEER.NOWACK@KIT.EDU
*Karlsruhe Institute of Technology*

**Jakob Runge** JAKOB.RUNGE@UNI-POTSDAM.DE
*University of Potsdam*

**David Rolnick** DROLNICK@MILA.QUEBEC
*Mila - Quebec AI Institute | McGill University*

**Editors:** Bijan Mazaheri and Niels Richard Hansen

## Abstract

Scientific research often seeks to understand the causal structure underlying high-level variables in a system. For example, climate scientists study how phenomena, such as El Niño, affect other climate processes at remote locations across the globe. However, scientists typically collect low-level measurements, such as geographically distributed temperature readings. From these, one needs to learn both a mapping to causally-relevant latent variables, such as a high-level representation of the El Niño phenomenon and other processes, as well as the causal model over them. The challenge is that this task, called causal representation learning, is highly underdetermined from observational data alone, requiring other constraints during learning to resolve the indeterminacies. In this work, we consider the task of partitioning observed variables into disentangled factors, such as extracting regions from geographically gridded measurement data in climate research or capturing brain regions from neural activity data. We demonstrate the identifiability of the resulting model and propose a differentiable method, *Causal Discovery with Single-parent Decoding* (CDSD), that simultaneously learns, from temporal data, the underlying latents and a causal graph over them. We assess the validity of our theoretical results using simulated data and showcase the practical validity of our method in an application to real-world data from the climate science field.

**Keywords:** Causal representation learning, identifiability, spatio-temporal data, climate science.

## 1. Introduction

In scientific domains, we often seek to learn causal relationships between high-level variables. For example, climate scientists want to understand how major modes of climate variability, such as the El Niño Southern Oscillation (ENSO) affect weather patterns worldwide (Runge et al., 2015, 2019a; Nowack et al., 2020). Neuroscientists want to uncover how different brain regions may be defined and influence one another (Reid et al., 2019). Identifying causal links in a network of correlations is challenging in itself, but to compound the difficulty, scientists typically collect low-level and noisy measurements in place of causally relevant high-level variables. For example, instead of recording the presence or absence of ENSO and its global impact, climate scientists measure sea-surface temperatures at many locations. Instead of measuring overall communication between brain regions, neuroscientists must work with proxy information such as blood flow or electrical activity in specific locations. Thus, scientific discovery requires causal representation learning: the coupled tasks of learning latent variables that represent semantically meaningful abstractions of the observed measurements and the quantification of causal relationships among these latents (Schölkopf et al., 2021).

What makes causal representation learning particularly challenging from a theoretical perspective is the non-identifiability of the models: there are typically many solutions – mappings from observations to latents – that fit the observed measurements equally well. Of these many alternatives, only some disentangled solutions capture the semantics of the true latents, while the other solutions entangle the latents, changing their semantics and making it impossible to then infer the causal relationships among the latents. As such, a key focus of causal representation learning is identifying the latents up to disentangled solutions using various inductive biases.

For spatial data with scientific applications, it is often useful to partition spatial locations of measurements to help us understand the system. For example, in climate science, spatial measurements such as sea-surface temperatures are commonly viewed as reflecting a limited set of geophysical processes that operate over coherent spatial zones.

In this paper, we introduce a causal representation learning method for temporal observations, *Causal Discovery with Single-parent Decoding* (CDSD), that, by partitioning observed variables, not only recovers disentangled latent variables, but also the causal graph over these variables. Learning a partitioning of the observations is equivalent to learning a mapping from latents to observations where each observed variable is a function of a single latent variable. We call this the *single-parent decoding* assumption. Related assumptions have given rise to interpretable latent variable models for gene expression (Bing et al., 2020), text (Arora et al., 2013), and brain imaging data (Monti and Hyvärinen, 2018). Our proposed model is particularly well suited to scientific applications such as climate science, where the sparse mapping corresponds to latent spatial zones that exhibit coherent weather patterns or climate trends.

We show that for the task of partitioning we can identify the latents up to some benign indeterminacies (e.g., permutations) as well as the temporal causal graph over the latents. We prove these identifiability results theoretically, and verify empirically that they hold in simulated data. Furthermore, we demonstrate the practical relevance of our method and assumptions via an application to a real-world climate science task. Our results indicate that CDSD successfully partitions climate variables into geographical regions and proposes plausible *teleconnections* between them – remote interactions between distant climate or weather states (Zhou et al., 2015) that have long been a target for climate scientists.

**Contributions.**

1. We propose a differentiable causal discovery approach that simultaneously learns both latent variables and a causal graph over the latents, based on time-series data. (Section 3)

2. We prove that the single-parent decoding assumption leads to the identifiability of both the latent representation and its causal graph. (Section 3.4, Theorem 2)

3. We evaluate our method both on synthetic data and a real-world climate science dataset in which relevant latents must be uncovered from measurements of sea-level pressure. (Section 4)

## 2. Related Work

**Causal discovery from time-series data.** Many causal discovery methods have been proposed for time-series data (Runge et al., 2019a, 2023). Constraint-based approaches, such as tsFCI (Entner and Hoyer, 2010), PCMCI+ (Runge, 2020) and TS-ICD (Rohekar et al., 2023), learn an equivalence class of directed acyclic graphs by iterative conditional independence testing. The proposed method is part of a line of work of score-based causal discovery methods that rely on a likelihood function to score each graph given the data. While standard score-based methods operate on a discrete search space of acyclic graphs (or Markov equivalence classes) that grows exponentially with the number of variables, continuous score-based methods enforce acyclicity only through a continuous acyclicity constraint, proposed by Zheng et al. (2018). Some variants of these methods have been proposed specifically to handle time-series data with instantaneous connections (Pamfil et al., 2020; Sun et al., 2021; Gao et al., 2022). However, in contrast with CDSD, all the methods mentioned above do not address the problem of learning a latent representation.

**Causal representation learning.** Recently, the field of causal representation learning (Schölkopf et al., 2021) has emerged with the goal of learning, from low-level data, representations that correspond to actionable quantities in a causal structure.[1] Since disentangling latent variables is impossible from independent and identically distributed samples (Hyvärinen and Pajunen, 1999; Locatello et al., 2019), existing works learn causal representations with weak supervision from paired samples (Ahuja et al., 2022b; Brehmer et al., 2022; Locatello et al., 2020; Von Kugelgen et al., 2021; Gresele et al., 2019), auxiliary labels (Khemakhem et al., 2020c,d; Lachapelle et al., 2023b; Hyvarinen and Morioka, 2017; Hyvarinen et al., 2019; Hyvarinen and Morioka, 2016), and temporal observations (Lachapelle et al., 2022; Lippe et al., 2022; Klindt et al., 2021; Yao et al., 2022a; Song et al., 2023; Yao et al., 2022b; Lachapelle et al., 2024), or by imposing constraints on the map from latents to observations (Taleb and Jutten, 1999; Gresele et al., 2021; Rhodes and Lee, 2021; Leeb et al., 2021; Moran et al., 2022; Buchholz et al., 2022; Zheng et al., 2022; Brady et al., 2023; Lachapelle et al., 2023a; Wiedemer et al., 2024; Brady et al., 2025). Wang et al. (2025) is the closest work to ours since it tackles the task of clustering spatial data. However, it assumes contiguous regions defined by spatial kernels (and focused on isotropic kernels in most experiments). In contrast, our proposed method do not assume any shape or structure to each block of the partition, which can be relevant in some fields like neurosciences, where a functional region might be distributed in space (Yeo et al.,

1. As a side note, the general idea of aggregating several low-level observations in order to only consider causal relationships at a high level is somewhat reminiscent of causal discovery with typed variables (Brouillard et al., 2022), *causal abstractions* (Rubenstein et al., 2017; Beckers et al., 2020) and *causal feature learning* (Chalupka et al., 2017) which was also applied to climate science (Chalupka et al., 2016).

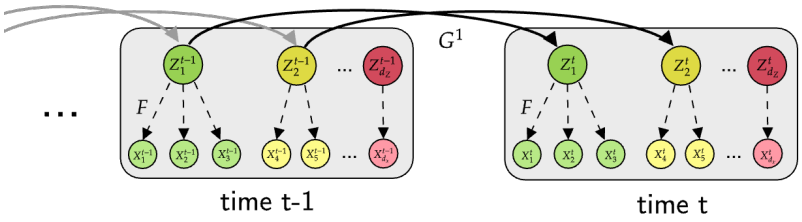


Figure 1: In the proposed generative model, the variables $\boldsymbol{z}$ are latent and $\boldsymbol{x}$ are observable variables. $G^k$ represents the connections between the latent variables, and $F$ the connections between the latents and the observables (dashed lines). The colors represent the different groups. For clarity, we illustrate here connections only up to $G^1$, but our method also leverages connections of higher order.

2011). We also note that, even without leveraging this assumption, our method was found to be highly competitive to Wang et al. (2025) for recovering latent variables.

The partitioning task supposes a single-parent structure that can be leveraged for identifiability. This is reminiscent of sparse decoding, which constrains each observed variable to be related to a sparse set of latent parents, either linearly (Chen et al., 2022; Monti and Hyvärinen, 2018; Bhattacharya and Dunson, 2011; Knowles and Ghahramani, 2011) or nonlinearly (Moran et al., 2022; Zheng et al., 2022; Rhodes and Lee, 2021) and, more specifically, to work on factor analysis (Silva et al., 2006; Monti and Hyvärinen, 2018; Xie et al., 2023; Kummerfeld and Ramsey, 2016). It also relates to the line of work on independent mechanism analysis (Gresele et al., 2021; Reizinger et al., 2022; Buchholz et al., 2022). Our identifiability result can be viewed as an instance of this broader family of sparsity-based identification conditions, specialized to the single-parent decoding setting induced by the partitioning task. We detail how our assumptions and conclusions relate to these prior results when presenting our theoretical analysis in Section 3.4.

Finally, this paper is also closely related to Varimax-PCMCI (Tibau et al., 2022) to which we directly compare CDSD in the experiments in Section 4. Varimax-PCMCI learns latent variables corresponding to regions and their causal relations. Unlike causal representation learning, this is performed in two separate stages: this method first applies *Principal Component Analysis* (PCA) and a Varimax rotation (Kaiser, 1958) to learn latent variables, as demonstrated in Nowack et al. (2020); Runge et al. (2015), and then applies PCMCI (Runge et al., 2019b), a temporal constraint-based causal discovery method, to recover the causal graph between the latents. In contrast, CDSD learns the latents and their temporal causal graph simultaneously via score-based structure learning, admitting nonlinearity in the relationships between latents as well as the mapping from latents to observations. Furthermore, while Varimax-PCMCI supports nonlinear relationships between the latents, it relies on nonlinear conditional independence tests, which do not scale well with dimensionality or sample size (Zhang et al., 2011; Strobl et al., 2019; Shah and Peters, 2020).

## 3. Causal Discovery with Single-Parent Decoding

We consider the time series model illustrated in Fig. 1. We observe $d_x$-dimensional variables $\{\boldsymbol{x}^t\}_{t=1}^T$ at $T$ time steps. The observed variables $\boldsymbol{x}^t$ are a function of $d_z$-dimensional latent variables $\boldsymbol{z}^t$. For example, the observations $\boldsymbol{x}^t$ might represent temperature measurements at $d_x$ grid locations

on Earth while each latent variable $\boldsymbol{z}_j^t$ might correspond to a high-level summary of temperature measurements in some unknown region to be discovered.

We consider a stationary time series of order $\tau$ (i.e., $\tau$ is the maximum number of past observations that can directly affect the current observation) over the latent variables $\boldsymbol{z}^1, \ldots, \boldsymbol{z}^T$. Thus, we describe the relationship between the latents at time $t$, $\boldsymbol{z}^t$, and those at each of the $\tau$ previous time steps using binary adjacency matrices $\{G^k\}_{k=0}^{\tau}$ that represent causal graphs between the latent variables and their past states. That is, each matrix $G^k \in \{0,1\}^{d_z \times d_z}$ encodes the presence of lagged relations between the timestep $t-k$ and the present timestep $t$, i.e., $G_{ij}^k = 1$ if and only if $z_j^{t-k}$ is a causal parent of $z_i^t$. To simplify presentation, we focus on a model without instantaneous causal relationships, i.e., the latents at time $t$ have no edges between one another in $G^0$. We show in Appendix H.1 how to practically support this case, and we even present validation experiments in this setting. We finally note that our identifiability results hold with instantaneous relations.

Finally, $F$ is the adjacency matrix of the bipartite causal graph with directed arrows from the latents $\boldsymbol{z}$ to the variables $\boldsymbol{x}$. We assume that $F$ has a specific structure: the *single-parent decoding* structure, where each variable $x_i$ has at most one latent parent. That is, the set of latent parents $\boldsymbol{z}_{pa_i^F}$ of each $x_i$, where $pa_i^F$ is the set of indices of the parents in graph $F$, is such that $|pa_i^F| \leq 1$.

### 3.1. Generative Model

We now describe the model in detail that can be used to generate synthetic data.

**Transition model.** The transition model defines the relations between the latent variables $\boldsymbol{z}$. We suppose that, at any given time step $t$, the latents are independent given their past:

$$p(\boldsymbol{z}^t \mid \boldsymbol{z}^{<t}) := \prod_{j=1}^{d_z} p(z_j^t \mid \boldsymbol{z}^{<t}), \tag{1}$$

where the notation $\boldsymbol{z}^{<t}$ is equivalent to $\boldsymbol{z}^{t-1}, \ldots, \boldsymbol{z}^{t-\tau}$. Each conditional is parameterized by a nonlinear function that depends on its parents:

$$p(z_j^t \mid \boldsymbol{z}^{<t}) := h(z_j^t;\ g_j(G_{j:}^1 \odot \boldsymbol{z}^{t-1}, \ldots, G_{j:}^\tau \odot \boldsymbol{z}^{t-\tau})), \tag{2}$$

where $h$ is a density function over $z_j^t$ parameterized by the output of the transition function $g_j$ which takes as input the causal parents of $z_j^t$ via a masking mechanism consisting of each $G_{j:}$ (the $j$-th row of the graph $G$) element-wise multiplying its corresponding past latent vector $\boldsymbol{z}$ ($\odot$ is the element-wise product). In our experiments, $h$ is a Gaussian density for its optimization convenience, though, our identifiability result (Theorem 1) requires only that $h$ has full support, leaving room for other choices.

**Observation model.** The observation model defines the relationship between the latent variables $\boldsymbol{z}$ and the observable variables $\boldsymbol{x}$. We assume conditional independence of the $x_j^t$:

$$p(\boldsymbol{x}^t \mid \boldsymbol{z}^t) := \prod_{j=1}^{d_x} p(x_j^t \mid \boldsymbol{z}_{pa_j^F}^t); \quad p(x_j^t \mid \boldsymbol{z}_{pa_j^F}^t) := \mathcal{N}(x_j^t; f_j(\boldsymbol{z}_{pa_j^F}^t), \sigma_j^2), \tag{3}$$

where $f_j : \mathbb{R} \to \mathbb{R}$, and $\boldsymbol{\sigma}^2 \in \mathbb{R}_{>0}^{d_x}$ are decoding functions. As previously mentioned, we assume a specific structure of $F$, namely that $|pa_j^F| \leq 1$ for all nodes $x_j$. In the next section, we will present a way to enforce this structure.

**Joint distribution.** The complete density of the model is thus given by:

$$p(\boldsymbol{x}^{\leq T}, \boldsymbol{z}^{\leq T}) := \prod_{t=1}^{T} p(\boldsymbol{z}^t \mid \boldsymbol{z}^{<t}) p(\boldsymbol{x}^t \mid \boldsymbol{z}^t)\,. \tag{4}$$

### 3.2. Evidence Lower Bound

The model can be fit by maximizing $p(\boldsymbol{x}^{\leq T}) = \int p(\boldsymbol{x}^{\leq T}, \boldsymbol{z}^{\leq T})\, d\boldsymbol{z}^{\leq T}$, which unfortunately involves an intractable integral. Instead, we rely on variational inference and optimize an *evidence lower bound* (ELBO) for $p(\boldsymbol{x}^{\leq T})$, as is common to many instantiations of temporal *variational auto-encoders* (VAEs) (see Girin et al. (2020) for a review).

We use $q(\boldsymbol{z}^{\leq T} \mid \boldsymbol{x}^{\leq T})$ as the variational approximation of the posterior $p(\boldsymbol{z}^{\leq T} \mid \boldsymbol{x}^{\leq T})$:

$$q(\boldsymbol{z}^{\leq T} \mid \boldsymbol{x}^{\leq T}) := \prod_{t=1}^{T} q(\boldsymbol{z}^t \mid \boldsymbol{x}^t); \quad q(\boldsymbol{z}^t \mid \boldsymbol{x}^t) := \mathcal{N}(\boldsymbol{z}^t; \tilde{\boldsymbol{f}}(\boldsymbol{x}^t), \mathrm{diag}(\tilde{\boldsymbol{\sigma}}^2)), \tag{5}$$

where $\tilde{\boldsymbol{f}} : \mathbb{R}^{d_x} \to \mathbb{R}^{d_z}$ and $\tilde{\boldsymbol{\sigma}}^2 \in \mathbb{R}^{d_z}_{>0}$ are the encoding functions.

Using the approximate posterior and the generative model from Section 3.1, we get the ELBO:

$$\log p(\boldsymbol{x}^{\leq T}) \geq \sum_{t=1}^{T} \Big[ \mathbb{E}_{\boldsymbol{z}^t \sim q(\boldsymbol{z}^t \mid \boldsymbol{x}^t)} \left[ \log p(\boldsymbol{x}^t \mid \boldsymbol{z}^t) \right] - \mathbb{E}_{\boldsymbol{z}^{<t} \sim q(\boldsymbol{z}^{<t} \mid \boldsymbol{x}^{<t})} \mathrm{KL} \left[ q(\boldsymbol{z}^t \mid \boldsymbol{x}^t) \,||\, p(\boldsymbol{z}^t \mid \boldsymbol{z}^{<t}) \right] \Big], \tag{6}$$

where KL stands for the Kullback-Leibler divergence. We show explicitly the derivation of this ELBO in Appendix A.

### 3.3. Inference

We now present some implementation choices and our optimization problem of interest, namely maximizing the ELBO defined in Equation 6 with respect to the different parameters of our generative model.

**Latent-to-observable graph.** We parameterize $F$, the graph between the latent $\boldsymbol{z}$ and the observable $\boldsymbol{x}$, using a weighted adjacency matrix $W \in \mathbb{R}^{d_x \times d_z}_{\geq 0}$. Put formally, $W_{ij} > 0$ if and only if $x_i$ is a child of $z_j$. In order to enforce the single-parent decoding assumption for $F$, we follow Monti and Hyvärinen (2018) and constrain $W$ to be non-negative and have columns that are orthonormal vectors.[2]

From these constraints our single-parent decoding assumption follows: at most one entry per row of $W$ can be non-zero, i.e., a given $x_i$ can have at most one parent. As stated earlier, these constraints on $W$ are essential since they ensure that the latent factors are identifiable up to permutation and invertible transformations (we elaborate on identifiability in Section 3.4).

**Encoding/decoding functions.** We parameterize the decoding functions $f_j$ in Equation 3 with a neural network $r_j$ whose input is filtered using $W$ as a mask: $f_j(\boldsymbol{z}^t_{pa_j^F}) = r_j(W_{j:}\boldsymbol{z}^t)$. For all experiments in the linear setting, we take $r_j$ to be the identity function as in Monti and Hyvärinen

2. Note that, to simplify, we will sometimes say that $W$ is *orthogonal* even if it is not a square matrix; by that, we specifically mean that its columns are orthonormal vectors.

(2018). The encoding function $\tilde{\boldsymbol{f}}$ (Equation 5) and the functions $g_j$ from the transition model (Equation 2) are also parameterized using neural networks.

**Continuous optimization.** We use $\boldsymbol{\phi}$ to denote the parameters of all neural networks ($r_j$, $g_j$, $\tilde{\boldsymbol{f}}$) and the learnable variance terms at Equations 3 and 5. To learn the graphs $G^k$ via continuous optimization, we use a similar approach to Ke et al. (2019); Brouillard et al. (2020); Ng et al. (2022b), where the graphs are sampled from distributions parameterized by $\Gamma^k \in \mathbb{R}^{d_z \times d_z}$ that are learnable parameters. Specifically, we use $G^k_{ij} \sim Bernoulli(\sigma(\Gamma^k_{ij}))$, where $\sigma(\cdot)$ is the sigmoid function. To simplify the notation, we use $G$ and $\Gamma$ as the sets $\{G^1, \dots, G^\tau\}$ and $\{\Gamma^1, \dots, \Gamma^\tau\}$ in the remainder of the presentation. This results in the following constrained optimization problem:

$$\begin{aligned} &\max_{W,\Gamma,\boldsymbol{\phi}} \mathbb{E}_{G\sim\sigma(\Gamma)}\left[\mathbb{E}_{\boldsymbol{x}}\left[\mathcal{L}_{\boldsymbol{x}}(W,\Gamma,\boldsymbol{\phi})\right]\right] - \lambda_s ||\sigma(\Gamma)||_1 \\ &\text{s.t. } W^\top W = I_{d_z} \text{ and } W_{i,j} \geq 0,\ \forall i,j\,, \end{aligned} \tag{7}$$

where $\mathcal{L}_{\boldsymbol{x}}$ is the ELBO corresponding to the right-hand side term in Equation 6, $\lambda_s > 0$ is a coefficient for the regularisation of the graph sparsity and $\sigma(\Gamma)$ is the tensor of all probabilities $\sigma(\Gamma^k_{ij})$. To enforce the non-negativity of $W$, we use the projected gradient on $\mathbb{R}_{\geq 0}$ (see Appendix C.2). As for the orthogonality of $W$, we enforce it using the following constraint:

$$h(W) := W^\top W - I_{d_z}\ .$$

We tackle the constrained optimization problem by using the *augmented Lagrangian method* (ALM), which amounts to performing gradient ascent-descent on the Lagrangian function augmented with an additional penalty term ((Nocedal and Wright, 1999); see Appendix C.1):

$$\underbrace{\mathbb{E}_{G\sim\sigma(\Gamma)}\left[\mathbb{E}_{\boldsymbol{x}}[\mathcal{L}_{\boldsymbol{x}}(W,\Gamma,\boldsymbol{\phi})]\right] - \lambda_s||\sigma(\Gamma)||_1 - \text{Tr}\left(\lambda_W^\top h(W)\right)}_{\text{Lagrangian function}} \underbrace{-\frac{\mu_W}{2}||h(W)||_2^2}_{\text{Penalty augmentation}}, \tag{8}$$

where $\lambda_W \in \mathbb{R}^{d_z \times d_z}$ form the matrix of Lagrangian multipliers (one multiplier for each constraint) and $\mu_W \in \mathbb{R}_{>0}$ is the coefficient of the penalty augmentation. Gradient ascent-descent alternates between taking (stochastic) gradient ascent steps w.r.t. $(W, \Gamma, \boldsymbol{\phi})$ and taking gradient descent steps w.r.t. $\lambda_W$. During this process, the penalty coefficient $\mu_W$ is also scheduled to increase as optimization proceeds.

To estimate the gradients w.r.t. the parameters $\Gamma$, we use the Gumbel-Softmax estimator (Maddison et al., 2017; Jang et al., 2017), which is a relaxation of the categorical distribution. This reparameterization trick was successfully used in several causal discovery methods (Kalainathan et al., 2018; Brouillard et al., 2020; Ng et al., 2022b; Lachapelle et al., 2024). For the ELBO optimization, we follow the classical VAE models (Kingma and Welling, 2013) by using the reparametrization trick and a closed-form expression for the KL divergence term since both $q(\boldsymbol{z}^t \mid \boldsymbol{x}^t)$ and $p(\boldsymbol{z}^t \mid \boldsymbol{z}^{<t})$ are multivariate Gaussians. Using these tricks we can learn the graphs $G$ and the matrix $W$ end-to-end.

When considering nonlinear decoding functions, we use a slightly different version where $W$ is, like $G$, a random matrix. For a more detailed exposition of this implementation and more details on the neural network's architecture, see Appendix E. To see how CDSD can support instantaneous relations, see Appendix H.1.

### 3.4. Identifiability Analysis

In this section, we discuss the identifiability of the model specified in Section 3.1. Put informally, we show that any solution that fits the ground-truth exactly recovers the true latents $\boldsymbol{z}^t$ up to permutation and coordinate-wise invertible transformations, i.e., transformations that preserve the semantics of the latents and admit valid causal discovery.

To formalize identifiability, we first state an important result that allows to show that two models expressing the same distribution over observations must have (i) the same decoder image and (ii) their latent representations related via a diffeomorphism. Similar results have been shown in previous literature (Khemakhem et al., 2020b; Lachapelle et al., 2022; Kivva et al., 2022; Ahuja et al., 2022a). For completeness, we state the result here and provide a proof in Appendix B. For conciseness, we use $\boldsymbol{f}, \boldsymbol{g}$ as the concatenations of functions $[f_1, \dots, f_{d_x}]$ and $[g_1, \dots, g_{d_z}]$.

**Proposition 1 (Identifiability of $\boldsymbol{f}$ and $p(\boldsymbol{z}^{\leq T})$ up to diffeomorphism)** *Assume we have two models $p(\boldsymbol{x}^{\leq T}, \boldsymbol{z}^{\leq T})$ and $\hat{p}(\boldsymbol{x}^{\leq T}, \hat{\boldsymbol{z}}^{\leq T})$ as specified in Section 3.1 with parameters $(\boldsymbol{g}, \boldsymbol{f}, G, \sigma^2)$ and $(\hat{\boldsymbol{g}}, \hat{\boldsymbol{f}}, \hat{G}, \hat{\sigma}^2)$, respectively. Assume further that $\boldsymbol{f}$ and $\hat{\boldsymbol{f}}$ are diffeomorphisms onto their respective images and that $d_z < d_x$ (we do not assume single-parent decoding). Therefore, whenever $\int p(\boldsymbol{x}^{\leq T}, \boldsymbol{z}^{\leq T}) d\boldsymbol{z}^{\leq T} = \int \hat{p}(\boldsymbol{x}^{\leq T}, \hat{\boldsymbol{z}}^{\leq T}) d\hat{\boldsymbol{z}}^{\leq T}$ for all $\boldsymbol{x}^{\leq T}$, we have $\boldsymbol{f}(\mathbb{R}^{d_z}) = \hat{\boldsymbol{f}}(\mathbb{R}^{d_z})$ and $\boldsymbol{v} := \boldsymbol{f}^{-1} \circ \hat{\boldsymbol{f}}$ is a diffeomorphism. Moreover, the density of the ground-truth latents $p(\boldsymbol{z}^{\leq T})$ and the density of the learned latents $\hat{p}(\hat{\boldsymbol{z}}^{\leq T})$ are related via*

$$p(\boldsymbol{v}(\hat{\boldsymbol{z}}^{\leq T})) \prod_{t=1}^{T} |\det D\boldsymbol{v}(\hat{\boldsymbol{z}}^t)| = \hat{p}(\hat{\boldsymbol{z}}^{\leq T}), \ \forall \hat{\boldsymbol{z}}^{\leq T} \in \mathbb{R}^{d_z \times T} .$$

Since the ELBO maximization is equivalent to minimizing a KL divergence, and assuming that our variational posterior is expressive enough, our learned model can match the data distribution, i.e., $\hat{p}(\boldsymbol{x}^{\leq T}) = p(\boldsymbol{x}^{\leq T})$. We now show how the structure of $F$ can be leveraged to establish that $\boldsymbol{v}$ corresponds only to a trivial indeterminacy.

**Identifiability via the single-parent structure of $F$.** The following proposition can be combined with Theorem 1 to show that the model specified in Section 3.1 with the single-parent decoding structure has a representation that is identifiable up to permutation and element-wise invertible transformations. The proof of this result can be found in Appendix B.

**Proposition 2 (Identifying latents of $\boldsymbol{f}$)** *Let $\boldsymbol{f} : \mathbb{R}^{d_z} \to \mathbb{R}^{d_x}$ and $\hat{\boldsymbol{f}} : \mathbb{R}^{d_z} \to \mathbb{R}^{d_x}$ be two diffeomorphisms onto their image $\boldsymbol{f}(\mathbb{R}^{d_z}) = \hat{\boldsymbol{f}}(\mathbb{R}^{d_z})$. Assume both $\boldsymbol{f}$ and $\hat{\boldsymbol{f}}$ have a single-parent decoding structure, i.e. $|pa_j^F| \leq 1$ and $|pa_j^{\hat{F}}| \leq 1$. Then, the map $\boldsymbol{v} := \boldsymbol{f}^{-1} \circ \hat{\boldsymbol{f}}$ has the following property: there exists a permutation $\pi$ such that, for all $i$, the function $\boldsymbol{v}_i(\boldsymbol{z})$ depends only on $\boldsymbol{z}_{\pi(i)}$.*

**Relation to previous identifiability results.** Our structural assumption of single-parent decoding is strictly more restrictive than assumptions used in some related identifiability results, which leverage decoder sparsity (Moran et al., 2022; Zheng et al., 2022; Brady et al., 2023), additivity (Lachapelle et al., 2023a), or orthogonality of the decoder Jacobian (Gresele et al., 2021; Reizinger et al., 2022; Buchholz et al., 2022). This stronger structural constraint, however, allows us to relax the accompanying "sufficient variability" assumptions. In this sense, our identifiability result strikes a new balance between structural assumptions and variability conditions that is particularly tailored to the task of partitioning.

**Identifiability of the latent causal graph $G$.** The above result, combined with Proposition 1, shows that we can identify the distribution $p(\boldsymbol{z}^{\leq T})$ up to permutation and trivial reparameterizations. A natural subsequent question is whether the latent causal graph $G$ can be identified from $p(\boldsymbol{z}^{\leq T})$, as studied in causal discovery. It is well-known that, in the absence of instantaneous causal connections, a temporal causal graph can be identified from the observational distribution (Peters et al., 2017, Theorem 10.1). Consequently, without instantaneous connections, the graph $G$ is identifiable (up to permutation) from $p(\boldsymbol{x}^{\leq T})$. In contrast, when instantaneous causal connections are allowed, the identifiability of the graph G is not guaranteed: at best, one can recover its Markov equivalence class, unless additional assumptions are imposed, such as additive noise models

## 4. Experiments

We empirically study the performance of CDSD on a number of linear and nonlinear settings using synthetic datasets. First, we compare CDSD to Varimax-PCMCI (Tibau et al., 2022), an alternate method that has a closely similar application. The results, reported at Section 4.1, show that CDSD is competitive with Varimax-PCMCI, especially in nonlinear settings. Next, we show with an ablation study that our constraint does empirically lead to a better recovery of the latent variables. Finally, we apply CDSD to a real-world climate science task and show that it recovers spatial aggregations related to known climate phenomena, such as the El Niño Southern Oscillation (Section 4.2).

An implementation of CDSD is available at `https://github.com/kurowasan/cdsd`. For Varimax-PCMCI, we follow the implementation of Tibau et al. (2022), where dimensionality reduction is done by combining PCA with a Varimax rotation (Kaiser, 1958), the causal graph is learned with PCMCI+ (Runge, 2020), and conditional independence is tested using a partial correlation test when latent dynamics are linear or the CMI-knn test (Runge, 2018) otherwise. Note that while PCMCI+ supports instantaneous connections, we always restrict the minimum time lag considered to 1. For further implementation details on both methods, refer to Appendix E.

### 4.1. Synthetic Data Benchmark

We first compare CDSD to Varimax-PCMCI on synthetic data. The key modeling components to evaluate in the two compared methods are: linear versus nonlinear dynamics in the learned causal graphs over latents, and linear versus nonlinear decoding functions from latents to observations. CDSD can flexibly handle all these settings, whereas Varimax-PCMCI assumes linear maps from latents to observations. We evaluate the methods in the following cases: 1) linear dynamics and linear decoding, 2) nonlinear dynamics and linear decoding, and 3) nonlinear decoding. We expect to find that CDSD shows clear advantages when the mappings from latents to observations are nonlinear. We also do an ablation study to show the identifiability gain induced by using the constraints on $W$ for data respecting the single-parent decoding assumption.

**Datasets.** We consider datasets randomly generated according to the model described at Section 3.1. The generative process is described in detail in Appendix D.1. Unless otherwise specified, we consider $T = 5000$ timesteps, a stationary process of order $\tau = 1$, $d_x = 100$ observed variables, $d_z = 10$ latent variables, and random latent dynamic graphs, akin to Erdős-Rényi graphs, with a probability $p = 0.15$ of including an edge. The nature of the relationships among latents – and from latents to observables – is either linear or nonlinear, depending on the specific experiment.

**Protocol.** We assess variability in each experimental condition by repeating each experiment 100 times with different randomly generated datasets. The hyperparameters of both methods are chosen

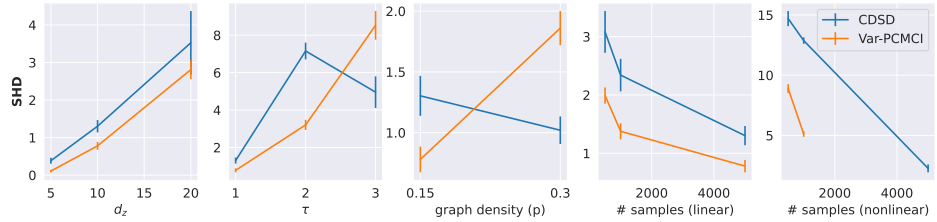


(*a*) (*b*)

Figure 2: Comparison of Varimax-PCMCI and CDSD in terms of SHD (lower is better) on simulated datasets with linear decoding and both a) linear and b) nonlinear latent dynamics.

to maximize overall performance on 10 randomly generated datasets distinct from the evaluation (see Appendix F). Note that, for both methods, $d_z$ and $\tau$ are not part of the hyperparameter search and are set to the ground-truth values in the generative process.

**Metrics.** Performance is assessed using two metrics: i) mean correlation coefficient (MCC), which measures the quality of the learned latent representation, and ii) structural Hamming distance (SHD), which measures the number of incorrect edges in the learned causal graph. MCC corresponds to the highest correlation coefficient between the estimated latents ($\hat{\boldsymbol{z}}$) and the ground-truth latent ($\boldsymbol{z}$) across all possible permutations (as described in (Khemakhem et al., 2020d)). The use of permutations is necessary since identification can only be guaranteed up to a permutation (see Section 3.4).

**1) Linear latent dynamics, Linear decoding.** We start by evaluating the methods in a context where all causal relationships are linear. We consider a variety of conditions: $d_z = \{5, 10, 20\}$, $\tau = \{1, 2, 3\}$, $T = \{500, 1000, 5000\}$, and $p = \{0.15, 0.3\}$ (which corresponds to sparse and dense graphs). We observed that both methods achieve a high MCC $\geq 0.95$, in all conditions, which is not surprising since they are both capable of identifying the latents when the decoding function is linear (see Appendix G.3). Since the variability across different datasets is high, we report the average SHD and its standard error in Fig. 2a. All differences are statistically significant, except for the condition $d_z = 20$ (see Appendix G.2). Varimax-PCMCI performs slightly better than CDSD in most conditions, except for more challenging cases such as stationary processes of greater order ($\tau = 3$) and denser graphs ($p = 0.3$). The latter result is in line with previous studies, which observed that continuous optimization methods tend to outperform their constraint-based counterparts in dense graphs (Zheng et al., 2018; Brouillard et al., 2020).

**2) Nonlinear latent dynamics, Linear decoding.** We now consider the case where causal relationships between the latents are nonlinear, while those from latents to observables remain linear. The results are reported at Fig. 2b. In contrast with the linear case, we do not present the results under all the experimental conditions due to the prohibitive running time of Varimax-PCMCI, which was greater than 24 hours for a single experiment (for the complete results, see Appendix G.3). This can be explained by its reliance on nonlinear conditional independence tests whose running time scales unfavorably w.r.t. the number of samples and variables (Runge, 2018; Zhang et al., 2018; Strobl et al., 2019). Consequently, results for Varimax-PCMCI are only reported up to 1000 samples. In sharp contrast, CDSD completed all experiments in a timely manner. Hence, while its solutions tend to have slightly higher SHD, CDSD can be used in contexts where Varimax-PCMCI, at least with a non-parametric conditional independence test, cannot.

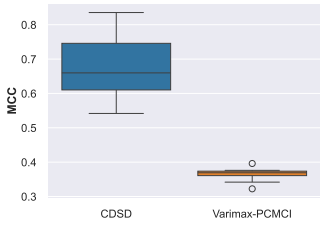


Figure 3: Comparison of CDSD and Varimax-PCMCI in terms of MCC (higher is better) on simulated datasets with nonlinear decoding.

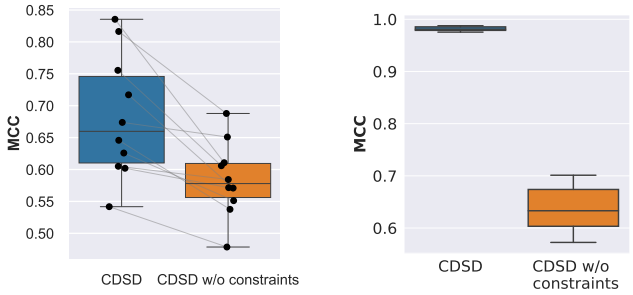


Figure 4: Ablation study comparing CDSD with and without the constraint on $W$. Respectively on nonlinear (left) and linear (right) decoding data.

**3) Nonlinear decoding.** The purpose of this experiment is to showcase the inability of Varimax-PCMCI to identify the latent representation when the relationships between the latents and the observables are nonlinear. This is the case, since PCA with a Varimax rotation is a linear dimension-reduction method. In contrast, CDSD should have no problem identifying the latents in this setting. We considered a dataset generated with the previously stated default conditions, where we ensure that the identifiability conditions of Section 3.4 are satisfied. The results are reported at Fig. 3. As expected, Varimax-PCMCI fails to recover the latent representation, achieving a poor MCC, while CDSD performs much better. These results clearly show the superiority of CDSD over Varimax-PCMCI when the relationships between latents and observables are nonlinear because of the linearity assumption in the PCA-Varimax step.

**Empirical validation of the identifiability result.** To empirically validate our identifiability result, we compare CDSD with an ablated version that does not enforce the non-negativity and orthogonality constraints on $W$ (see Equation 7). Fig. 4 reports the average MCC on 10 datasets in the default experimental conditions with nonlinear mixing (left) and linear mixing (right). In line with the theoretical results of Section 3.4, the MCC clearly shows that the constraint on $W$ is essential for recovering a good representation. In the nonlinear mixing setting, the datasets exhibit substantial variability, so we additionally report the paired MCC differences. For every dataset, CDSD with the constraint achieves a higher MCC than the unconstrained variant (this difference is statistically significant, Appendix G.2). In the linear mixing case, the effect is even more pronounced: the constrained version yields near-perfect recovery, with MCC values approaching 1.

### 4.2. Real-world Application to Climate Science

To test the capabilities of CDSD in real-world settings, we apply it to the National Oceanic and Atmospheric Administration's (NOAA) *Reanalysis 1 mean sea-level pressure (MSLP)* dataset (Kalnay et al., 1996). Local variations in MSLP reflect changes in the dynamical state of the atmosphere for a certain region or, in other words, the occurrence and passing of weather systems (e.g. low- or high-pressure systems). Over time, MSLP data can thus be used to identify regions that share common weather properties, and to understand how regional weather systems are coupled to each other globally. Identifying such causal relationships would help climate scientists to better understand Earth's global dynamical weather system and could provide leverage for data-driven forecasting systems.

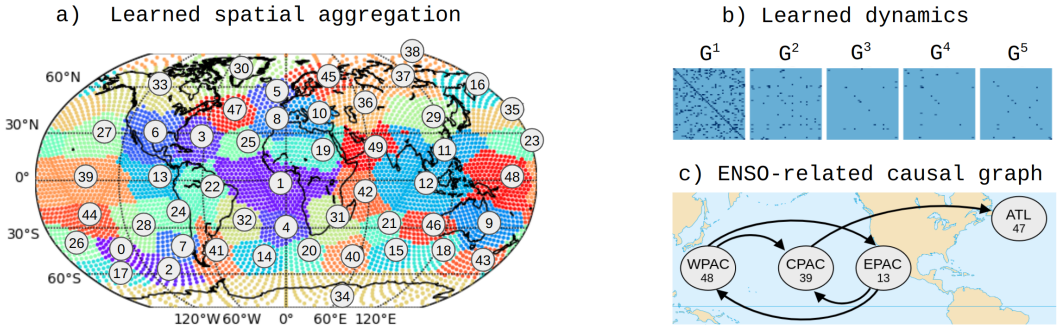


Figure 5: Overview of the climate science results for CDSD. a) Segmentation of the Earth's surface according to $W$. The groups are colored and numbered based on the latent variable to which they are related. b) Adjacency matrices for latent dynamic graphs $G^1, \ldots, G^5$, shown as $d_z \times d_z$ heatmaps. c) Subgraph of $G^1$ showing the learned causal relationships between known ENSO-related regions.

Here, we use MSLP data from 1948–2022 on a global regular grid with a resolution of $2.5°$ longitude $\times$ $2.5°$ latitude. We aggregated the daily time-series to weekly data and regridded it onto an icosahedral-hexagonal grid (see Appendix D.2) (Majewski et al., 2002). The resulting dimensions are $3900 \times 6250$, covering 52 weeks of 75 years ($T = 3900$) and $d_x = 6250$ grid cells. We apply CDSD in order to cluster regions of similar weather properties, and identify which regions are causally linked to weather phenomena in other regions. We use the method with linear dynamics and linear decoding, and, similarly to (Runge et al., 2015), we use $d_z = 50$ and $\tau = 5$.

Fig. 5a shows the learned spatial aggregations and the causal graph $G$ obtained with CDSD. The learned aggregations match well with the coarser climatological regions used in the latest climate change assessment reports of the Intergovernmental Panel on Climate Change (IPCC), which were manually defined (compare to Figure 1 in Iturbide et al. (2020)). The learned clusters broadly reflect a superposition of the effects of transport timescales, ocean-to-land boundaries, and the zonal and meridional patterns of the tropospheric circulation (Hadley, Ferrel, and polar cells) in both hemispheres. Among the visually most prominent features is the identification of East Pacific, Central Pacific, and Western Pacific clusters (clusters 13, 39, 48) along the tropical Pacific. These zones are well-known to be coupled through ENSO, but the East Pacific typically sees the most pronounced temperature oscillations due to its shallow oceanic thermocline (e.g., Nowack et al., 2017). We also recover a relatively zonal structure of clusters in the Southern Hemisphere mid-latitudes (clusters 17, 2, 41, 14, 20, 40, 15, 18, and 43 from west to east) where the zonal tropospheric circulation moves relatively freely without significant disturbances from land boundaries. While not strictly enforced, the learned regions are spatially connected/homogeneous, i.e. not divided into several de-localized parts (see Appendix G.4). Highly de-localized, globally distributed, components are for example a major issue in interpreting standard principal component analyses of MSLP data (Hannachi et al., 2007). In contrast, the regions learned by CDSD without constraints are not localized and are harder to associate to known regions such as those related to ENSO (see Appendix G.4).

While a detailed analysis of the learned causal graphs (Fig. 5b) is beyond the scope of this study, it is intuitive that the strongest and most frequent connections are found within a timescale of one week ($G^1$), but notably longer - likely more distant connections - are found, too. These likely reflect the well-known presence of long-distance teleconnections between world regions (Nowack et al.,

2020). In Fig. 5c we show one example of the causal coupling inferred for ENSO-related modes (clusters 13, 39, 47, 48) which is similar to the causal graph found in Runge et al. (2019b).

## 5. Discussion

We presented CDSD, which learns a partitioning and a causal representation along with its connectivity from time series data. The method is accompanied by theoretical results that guarantee the identifiability of the representation up to benign transformations. The key benefits of CDSD over Varimax-PCMCI are that i) it supports nonlinear decoding functions, and ii) as opposed to its constraint-based tests, it scales well in the number of samples and variables in the nonlinear dynamics case. Furthermore, as illustrated in the application to climate science, CDSD and its assumptions, appear to be applicable in practice and seem particularly well-suited for problems of scientific interest, such as the spatial clustering of weather measurements.

We highlight a few limitations that should be taken into account. Some of our assumptions, such as the stationarity of the dynamical system and the absence of latent confounders, can be partially or totally violated in real-world applications. We did not study the impact of model misspecifications on the performance of CDSD. In all our experiments, we assumed that $d_z$ and $\tau$ were known. However, in practical applications, these values are unknown and might be difficult to infer, even for experts. One practical remedy can be model selection: training models across a range of $d_z$ values and retaining the one with the highest ELBO on held-out data. Stability-based criteria such as UDR (Duan et al., 2019) can also diagnose whether the learned representations are robust to random initializations, where a failure would suggest an inappropriate $d_z$.

Besides these limitations, CDSD, in its general form, can be applied in several contexts or readily extended. The framework has already seen adoption beyond this work: Boussard et al. (2023) applied it to additional physical variables across diverse climate modalities, and Hickman et al. (2025) incorporated Bayesian filtering to stabilize long-term autoregressive emulation. We emphasize that the method supports instantaneous connections (see Appendix H.1). It can also be used with multivariate data (e.g., in climate science applications, one could be interested in modeling sea-level pressure, but also temperature, precipitation, etc.). Furthermore, in other contexts, such as brain imaging studies, one could be interested in learning different graphs $G$ for different subjects, while sharing a common spatial aggregation (as in Monti and Hyvärinen (2018)). The method can also be adapted to learn from both observational and interventional data. In Appendix H, we show how our method can be adapted to support all these settings. Overall, we believe that CDSD is a significant step toward the goal of bridging the gap between causal representation learning and scientific applications.

## Acknowledgments

PB acknowledges the support of the Natural Sciences and Engineering Research Council of Canada (NSERC) and acknowledges Xavier-Andoni Tibau for helpful discussions regarding the Varimax-PCMCI method. PN was supported by the UK Natural Environment Research Council, grant number NE/V012045/1, and the Chair for AI in Climate and Environmental Sciences at KIT. JR has received funding from the European Research Council (ERC) Starting Grant CausalEarth under the European Union's Horizon 2020 research and innovation program (Grant Agreement No. 948112). This project was supported by the Intel-Mila partnership program and the Canada CIFAR AI Chairs program.

## REFERENCES

Kartik Ahuja, Jason Hartford, and Yoshua Bengio. Properties from mechanisms: an equivariance perspective on identifiable representation learning. In *International Conference on Learning Representations*, 2022a.

Kartik Ahuja, Jason Hartford, and Yoshua Bengio. Weakly supervised representation learning with sparse perturbations. In *Advances in Neural Information Processing Systems*, 2022b.

TW Anderson and Herman Rubin. Statistical inference in. In *Proceedings of the Third Berkeley Symposium on Mathematical Statistics and Probability: Held at the Statistical Laboratory, University of California, December, 1954, July and August, 1955*, volume 1, page 111. Univ of California Press, 1956.

Sanjeev Arora, Rong Ge, Yonatan Halpern, David Mimno, Ankur Moitra, David Sontag, Yichen Wu, and Michael Zhu. A practical algorithm for topic modeling with provable guarantees. In *International conference on machine learning*, 2013.

Sander Beckers, Frederick Eberhardt, and Joseph Y Halpern. Approximate causal abstractions. In *Uncertainty in Artificial Intelligence*, pages 606–615. PMLR, 2020.

Anirban Bhattacharya and David B Dunson. Sparse bayesian infinite factor models. *Biometrika*, 98 (2):291–306, 2011.

Xin Bing, Florentina Bunea, Yang Ning, and Marten Wegkamp. Adaptive estimation in structured factor models with applications to overlapping clustering. *Annals of Statistics*, 48(4), 2020.

Julien Boussard, Chandni Nagda, Julia Kaltenborn, Charlotte Emilie Elektra Lange, Philippe Brouillard, Yaniv Gurwicz, Peer Nowack, and David Rolnick. Towards causal representations of climate model data. *arXiv preprint arXiv:2312.02858*, 2023.

J. Brady, R. S. Zimmermann, Y. Sharma, B. Schölkopf, J. von Kügelgen, and W. Brendel. Provably learning object-centric representations. In *International Conference on Machine Learning*, 2023.

Jack Brady, Julius von Kügelgen, Sebastien Lachapelle, Simon Buchholz, Thomas Kipf, and Wieland Brendel. Interaction asymmetry: A general principle for learning composable abstractions. In *The Thirteenth International Conference on Learning Representations*, 2025.

Johann Brehmer, Pim De Haan, Phillip Lippe, and Taco Cohen. Weakly supervised causal representation learning. *Advances in Neural Information Processing Systems*, 2022.

Philippe Brouillard, Sébastien Lachapelle, Alexandre Lacoste, Simon Lacoste-Julien, and Alexandre Drouin. Differentiable causal discovery from interventional data. *Advances in Neural Information Processing Systems*, 33:21865–21877, 2020.

Philippe Brouillard, Perouz Taslakian, Alexandre Lacoste, Sébastien Lachapelle, and Alexandre Drouin. Typing assumptions improve identification in causal discovery. In *Conference on Causal Learning and Reasoning*, pages 162–177. PMLR, 2022.

Simon Buchholz, Michel Besserve, and Bernhard Schölkopf. Function classes for identifiable nonlinear independent component analysis. *Advances in Neural Information Processing Systems*, 35:16946–16961, 2022.

Krzysztof Chalupka, Tobias Bischoff, Pietro Perona, and Frederick Eberhardt. Unsupervised discovery of el nino using causal feature learning on microlevel climate data. *arXiv preprint arXiv:1605.09370*, 2016.

Krzysztof Chalupka, Frederick Eberhardt, and Pietro Perona. Causal feature learning: an overview. *Behaviormetrika*, 44(1):137–164, 2017.

Zhengming Chen, Feng Xie, Jie Qiao, Zhifeng Hao, Kun Zhang, and Ruichu Cai. Identification of linear latent variable model with arbitrary distribution. In *Proceedings of the AAAI Conference on Artificial Intelligence*, volume 36, pages 6350–6357, 2022.

C Dey, C Sanders, J Clochard, and J Hennessy. Guide to the wmo table driven code form used for the representation and exchange of regularly spaced data in binary form: Fm 92 grib. Technical report, WMO Tech. Rep., 98 pp.[Available online at http://www. wmo. int/pages/prog . . . , 2007.

Sunny Duan, Loic Matthey, Andre Saraiva, Nicholas Watters, Christopher P Burgess, Alexander Lerchner, and Irina Higgins. Unsupervised model selection for variational disentangled representation learning. *arXiv preprint arXiv:1905.12614*, 2019.

Doris Entner and Patrik O Hoyer. On causal discovery from time series data using fci. *Probabilistic graphical models*, pages 121–128, 2010.

Tian Gao, Debarun Bhattacharjya, Elliot Nelson, Miao Liu, and Yue Yu. Idyno: Learning nonparametric dags from interventional dynamic data. In *International Conference on Machine Learning*, pages 6988–7001. PMLR, 2022.

Laurent Girin, Simon Leglaive, Xiaoyu Bie, Julien Diard, Thomas Hueber, and Xavier Alameda-Pineda. Dynamical variational autoencoders: A comprehensive review. *arXiv preprint arXiv:2008.12595*, 2020.

L. Gresele, P. K. Rubenstein, A. Mehrjou, F. Locatello, and B. Scholkopf. The incomplete rosetta stone problem identifiability results for multi-view nonlinear ICA. In *Conference on Uncertainty in Artificial Intelligence*, 2019.

Luigi Gresele, Julius Von Kügelgen, Vincent Stimper, Bernhard Schölkopf, and Michel Besserve. Independent mechanism analysis, a new concept? *Advances in neural information processing systems*, 34:28233–28248, 2021.

Abdel Hannachi, Ian T Jolliffe, and David B Stephenson. Empirical orthogonal functions and related techniques in atmospheric science: A review. *International Journal of Climatology: A Journal of the Royal Meteorological Society*, 27(9):1119–1152, 2007.

Sebastian Hickman, Ilija Trajkovic, Julia Kaltenborn, Francis Pelletier, Alex Archibald, Yaniv Gurwicz, Peer Nowack, David Rolnick, and Julien Boussard. Causal climate emulation with bayesian filtering. *arXiv preprint arXiv:2506.09891*, 2025.

Geoffrey Hinton, Nitish Srivastava, and Kevin Swersky. Neural networks for machine learning lecture 6a overview of mini-batch gradient descent. *Cited on*, 14(8):2, 2012.

Harold Hotelling. Analysis of a complex of statistical variables into principal components. *Journal of educational psychology*, 24(6):417, 1933.

S. Hoyer and J. Hamman. xarray: N-D labeled arrays and datasets in Python. *In revision, J. Open Res. Software*, 2017.

Aapo Hyvarinen and Hiroshi Morioka. Unsupervised feature extraction by time-contrastive learning and nonlinear ica. *Advances in Neural Information Processing Systems*, 2016.

Aapo Hyvarinen and Hiroshi Morioka. Nonlinear ICA of Temporally Dependent Stationary Sources. *The 20th International Conference on Artificial Intelligence and Statistics*, 2017.

Aapo Hyvärinen and Petteri Pajunen. Nonlinear independent component analysis: Existence and uniqueness results. *Neural networks*, 12(3):429–439, 1999.

Aapo Hyvarinen, Hiroaki Sasaki, and Richard E Turner. Nonlinear ICA Using Auxiliary Variables and Generalized Contrastive Learning. *The 22nd International Conference on Artificial Intelligence and Statistics*, 2019.

Maialen Iturbide, José M Gutiérrez, Lincoln M Alves, Joaquín Bedia, Ruth Cerezo-Mota, Ezequiel Cimadevilla, Antonio S Cofiño, Alejandro Di Luca, Sergio Henrique Faria, Irina V Gorodetskaya, et al. An update of ipcc climate reference regions for subcontinental analysis of climate model data: definition and aggregated datasets. *Earth System Science Data*, 12(4):2959–2970, 2020.

E. Jang, S. Gu, and B. Poole. Categorical reparameterization with gumbel-softmax. *Proceedings of the 34th International Conference on Machine Learning*, 2017.

Richard Arnold Johnson, Dean W Wichern, et al. Applied multivariate statistical analysis. 2002.

Philip W Jones. First-and second-order conservative remapping schemes for grids in spherical coordinates. *Monthly Weather Review*, 127(9):2204–2210, 1999.

Henry F Kaiser. The varimax criterion for analytic rotation in factor analysis. *Psychometrika*, 23(3): 187–200, 1958.

Diviyan Kalainathan, Olivier Goudet, Isabelle Guyon, David Lopez-Paz, and Michèle Sebag. Sam: Structural agnostic model, causal discovery and penalized adversarial learning. 2018.

Eugenia Kalnay, Masao Kanamitsu, Robert Kistler, William Collins, Dennis Deaven, Lev Gandin, Mark Iredell, Suranjana Saha, Glenn White, John Woollen, et al. The ncep/ncar 40-year reanalysis project. *Bulletin of the American meteorological Society*, 77(3):437–472, 1996.

Nan Rosemary Ke, Olexa Bilaniuk, Anirudh Goyal, Stefan Bauer, Hugo Larochelle, Bernhard Schölkopf, Michael C Mozer, Chris Pal, and Yoshua Bengio. Learning neural causal models from unknown interventions. *arXiv preprint arXiv:1910.01075*, 2019.

I. Khemakhem, R. Monti, D. Kingma, and A. Hyvärinen. Ice-beem identifiable conditional energy-based deep models based on nonlinear ica. In *Advances in Neural Information Processing Systems*, 2020a.

Ilyes Khemakhem, Diederik Kingma, Ricardo Monti, and Aapo Hyvarinen. Variational autoencoders and nonlinear ica: A unifying framework. *Proceedings of the Twenty Third International Conference on Artificial Intelligence and Statistics*, 2020b.

Ilyes Khemakhem, Diederik Kingma, Ricardo Monti, and Aapo Hyvarinen. Variational autoencoders and nonlinear ica: A unifying framework. In *International Conference on Artificial Intelligence and Statistics*, pages 2207–2217. PMLR, 2020c.

Ilyes Khemakhem, Ricardo Monti, Diederik Kingma, and Aapo Hyvarinen. Ice-beem: Identifiable conditional energy-based deep models based on nonlinear ica. *Advances in Neural Information Processing Systems*, 33:12768–12778, 2020d.

Diederik P Kingma and Max Welling. Auto-encoding variational bayes. *arXiv preprint arXiv:1312.6114*, 2013.

Bohdan Kivva, Goutham Rajendran, Pradeep Ravikumar, and Bryon Aragam. Identifiability of deep generative models without auxiliary information. In *Advances in Neural Information Processing Systems*, 2022.

David A. Klindt, Lukas Schott, Yash Sharma, Ivan Ustyuzhaninov, Wieland Brendel, Matthias Bethge, and Dylan Paiton. Towards nonlinear disentanglement in natural data with temporal sparse coding. In *International Conference on Learning Representations*, 2021.

David Knowles and Zoubin Ghahramani. Nonparametric bayesian sparse factor models with application to gene expression modeling. *Annals of Applied Statistics*, 2011.

Erich Kummerfeld and Joseph Ramsey. Causal clustering for 1-factor measurement models. In *Proceedings of the 22nd ACM SIGKDD international conference on knowledge discovery and data mining*, pages 1655–1664, 2016.

S. Lachapelle, D. Mahajan, I. Mitliagkas, and S. Lacoste-Julien. Additive decoders for latent variables identification and cartesian-product extrapolation. In *Advances in Neural Information Processing Systems*, 2023a.

Sebastien Lachapelle, Pau Rodriguez, Yash Sharma, Katie E Everett, Rémi LE PRIOL, Alexandre Lacoste, and Simon Lacoste-Julien. Disentanglement via mechanism sparsity regularization: A new principle for nonlinear ICA. In *First Conference on Causal Learning and Reasoning*, 2022.

Sébastien Lachapelle, Tristan Deleu, Divyat Mahajan, Ioannis Mitliagkas, Yoshua Bengio, Simon Lacoste-Julien, and Quentin Bertrand. Synergies between disentanglement and sparsity: Generalization and identifiability in multi-task learning. *International Conference on Machine Learning*, 2023b.

Sébastien Lachapelle, Pau Rodríguez López, Yash Sharma, Katie Everett, Rémi Le Priol, Alexandre Lacoste, and Simon Lacoste-Julien. Nonparametric partial disentanglement via mechanism sparsity: Sparse actions, interventions and sparse temporal dependencies, 2024.

F. Leeb, G. Lanzillotta, Y. Annadani, M. Besserve, S. Bauer, and B. Schölkopf. Structure by architecture: Disentangled representations without regularization, 2021.

Anson Lei, Bernhard Schölkopf, and Ingmar Posner. Variational causal dynamics: Discovering modular world models from interventions. *arXiv preprint arXiv:2206.11131*, 2022.

Yehua Li and Marc G Genton. Single-index additive vector autoregressive time series models. *Scandinavian Journal of Statistics*, 36(3):369–388, 2009.

Phillip Lippe, Sara Magliacane, Sindy Löwe, Yuki M. Asano, Taco Cohen, and Efstratios Gavves. CITRIS: Causal Identifiability from Temporal Intervened Sequences. *International Conference on Machine Learning (ICML)*, 2022.

Francesco Locatello, Stefan Bauer, Mario Lucic, Gunnar Raetsch, Sylvain Gelly, Bernhard Schölkopf, and Olivier Bachem. Challenging common assumptions in the unsupervised learning of disentangled representations. In *international conference on machine learning*, pages 4114–4124. PMLR, 2019.

Francesco Locatello, Ben Poole, Gunnar Rätsch, Bernhard Schölkopf, Olivier Bachem, and Michael Tschannen. Weakly-supervised disentanglement without compromises. In *International Conference on Machine Learning*, 2020.

C. J. Maddison, A. Mnih, and Y. W. Teh. The concrete distribution: A continuous relaxation of discrete random variables. *Proceedings of the 34th International Conference on Machine Learning*, 2017.

Detlev Majewski. The new global icosahedral-hexagonal gridpoint model gme of the deutscher wetterdienst. In *Procceding of a Seminar held at ECMWF on Recent Developments in Numberical Methods for Atmospheric Modelling, 1998*, pages 172–201, 1998.

Detlev Majewski, Dörte Liermann, Peter Prohl, Bodo Ritter, Michael Buchhold, Thomas Hanisch, Gerhard Paul, Werner Wergen, and John Baumgardner. The operational global icosahedral–hexagonal gridpoint model gme: Description and high-resolution tests. *Monthly Weather Review*, 130(2):319–338, 2002.

Ricardo Pio Monti and Aapo Hyvärinen. A unified probabilistic model for learning latent factors and their connectivities from high-dimensional data. *arXiv preprint arXiv:1805.09567*, 2018.

Gemma E Moran, Dhanya Sridhar, Yixin Wang, and David M Blei. Identifiable variational autoencoders via sparse decoding. *Transactions of Machine Learning Research*, 2022.

Ignavier Ng, Sébastien Lachapelle, Nan Rosemary Ke, Simon Lacoste-Julien, and Kun Zhang. On the convergence of continuous constrained optimization for structure learning. In *International Conference on Artificial Intelligence and Statistics*, pages 8176–8198. PMLR, 2022a.

Ignavier Ng, Shengyu Zhu, Zhuangyan Fang, Haoyang Li, Zhitang Chen, and Jun Wang. Masked gradient-based causal structure learning. In *Proceedings of the 2022 SIAM International Conference on Data Mining (SDM)*, pages 424–432. SIAM, 2022b.

Jorge Nocedal and Stephen J Wright. *Numerical optimization*. Springer, 1999.

P. J. Nowack, P. Braesicke, N. L. Abraham, and J. A. Pyle. On the role of ozone feedback in the enso amplitude response under global warming. *Geophysical Research Letters*, 44:3858–3866, 2017.

Peer Nowack, Jakob Runge, Veronika Eyring, and Joanna D Haigh. Causal networks for climate model evaluation and constrained projections. *Nature communications*, 11(1):1415, 2020.

Roxana Pamfil, Nisara Sriwattanaworachai, Shaan Desai, Philip Pilgerstorfer, Konstantinos Georgatzis, Paul Beaumont, and Bryon Aragam. Dynotears: Structure learning from time-series data. In *International Conference on Artificial Intelligence and Statistics*, pages 1595–1605. PMLR, 2020.

Karl Pearson. Liii. on lines and planes of closest fit to systems of points in space. *The London, Edinburgh, and Dublin philosophical magazine and journal of science*, 2(11):559–572, 1901.

J. Peters, D. Janzing, and B. Schölkopf. *Elements of Causal Inference - Foundations and Learning Algorithms*. MIT Press, 2017.

Trang Van Pham, Christian Steger, Burkhardt Rockel, Klaus Keuler, Ingo Kirchner, Mariano Mertens, Daniel Rieger, Günther Zängl, and Barbara Früh. Icon in climate limited-area mode (icon release version 2.6. 1): a new regional climate model. *Geoscientific Model Development*, 14(2):985–1005, 2021.

D. Pollard. *A User's Guide to Measure Theoretic Probability*. Cambridge University Press, 2001.

James Ramsay and Bernard Silverman. Applied functional data analysis: methods and case studies. 2007.

Andrew T Reid, Drew B Headley, Ravi D Mill, Ruben Sanchez-Romero, Lucina Q Uddin, Daniele Marinazzo, Daniel J Lurie, Pedro A Valdés-Sosa, Stephen José Hanson, Bharat B Biswal, et al. Advancing functional connectivity research from association to causation. *Nature neuroscience*, 22(11):1751–1760, 2019.

Patrik Reizinger, Luigi Gresele, Jack Brady, Julius Von Kügelgen, Dominik Zietlow, Bernhard Schölkopf, Georg Martius, Wieland Brendel, and Michel Besserve. Embrace the gap: Vaes perform independent mechanism analysis. *Advances in Neural Information Processing Systems*, 35:12040–12057, 2022.

Travers Rhodes and Daniel Lee. Local disentanglement in variational auto-encoders using jacobian $l\_1$ regularization. *Advances in Neural Information Processing Systems*, 34:22708–22719, 2021.

Raanan Y Rohekar, Shami Nisimov, Yaniv Gurwicz, and Gal Novik. From temporal to contemporaneous iterative causal discovery in the presence of latent confounders. *Proceedings of the 40th International Conference on Machine Learning*, 2023.

Paul K Rubenstein, Sebastian Weichwald, Stephan Bongers, Joris M Mooij, Dominik Janzing, Moritz Grosse-Wentrup, and Bernhard Schölkopf. Causal consistency of structural equation models. *arXiv preprint arXiv:1707.00819*, 2017.

Jakob Runge. Conditional independence testing based on a nearest-neighbor estimator of conditional mutual information. In *International Conference on Artificial Intelligence and Statistics*, pages 938–947. PMLR, 2018.

Jakob Runge. Discovering contemporaneous and lagged causal relations in autocorrelated nonlinear time series datasets. In *Conference on Uncertainty in Artificial Intelligence*, pages 1388–1397. PMLR, 2020.

Jakob Runge, Vladimir Petoukhov, Jonathan F Donges, Jaroslav Hlinka, Nikola Jajcay, Martin Vejmelka, David Hartman, Norbert Marwan, Milan Paluš, and Jürgen Kurths. Identifying causal gateways and mediators in complex spatio-temporal systems. *Nature communications*, 6(1):1–10, 2015.

Jakob Runge, Sebastian Bathiany, Erik Bollt, Gustau Camps-Valls, Dim Coumou, Ethan Deyle, Clark Glymour, Marlene Kretschmer, Miguel D Mahecha, Jordi Muñoz-Marí, et al. Inferring causation from time series in earth system sciences. *Nature communications*, 10(1):1–13, 2019a.

Jakob Runge, Peer Nowack, Marlene Kretschmer, Seth Flaxman, and Dino Sejdinovic. Detecting and quantifying causal associations in large nonlinear time series datasets. *Science advances*, 5 (11):eaau4996, 2019b.

Jakob Runge, Andreas Gerhardus, Gherardo Varando, Veronika Eyring, and Gustau Camps-Valls. Causal inference for time series. *Nature Reviews Earth & Environment*, 10:2553, 2023.

Kevin Sahr, Denis White, and A Jon Kimerling. Geodesic discrete global grid systems. *Cartography and Geographic Information Science*, 30(2):121–134, 2003.

Bernhard Schölkopf, Francesco Locatello, Stefan Bauer, Nan Rosemary Ke, Nal Kalchbrenner, Anirudh Goyal, and Yoshua Bengio. Toward causal representation learning. *Proceedings of the IEEE*, 109(5):612–634, 2021.

Uwe Schulzweida. Cdo user guide, October 2022. URL https://doi.org/10.5281/zenodo.7112925.

Rajen D Shah and Jonas Peters. The hardness of conditional independence testing and the generalised covariance measure. *The Annals of Statistics*, 48(3):1514–1538, 2020.

Ricardo Silva, Richard Scheines, Clark Glymour, Peter Spirtes, and David Maxwell Chickering. Learning the structure of linear latent variable models. *Journal of Machine Learning Research*, 7 (2), 2006.

Xiangchen Song, Weiran Yao, Yewen Fan, Xinshuai Dong, Guangyi Chen, Juan Carlos Niebles, Eric Xing, and Kun Zhang. Temporally disentangled representation learning under unknown nonstationarity. *Advances in Neural Information Processing Systems*, 36:8092–8113, 2023.

E. V. Strobl, K. Zhang, and S. Visweswaran. Approximate kernel-based conditional independence tests for fast non-parametric causal discovery. *Journal of Causal Inference*, 2019.

Xiangyu Sun, Guiliang Liu, Pascal Poupart, and Oliver Schulte. Nts-notears: Learning nonparametric temporal dags with time-series data and prior knowledge. *arXiv preprint arXiv:2109.04286*, 2021.

A. Taleb and C. Jutten. Source separation in post-nonlinear mixtures. *IEEE Transactions on Signal Processing*, 1999.

Xavier-Andoni Tibau, Christian Reimers, Andreas Gerhardus, Joachim Denzler, Veronika Eyring, and Jakob Runge. A spatiotemporal stochastic climate model for benchmarking causal discovery methods for teleconnections. *Environmental Data Science*, 1:e12, 2022.

Martin Vejmelka, Lucie Pokorná, Jaroslav Hlinka, David Hartman, Nikola Jajcay, and Milan Paluš. Non-random correlation structures and dimensionality reduction in multivariate climate data. *Climate Dynamics*, 44:2663–2682, 2015.

J. Von Kugelgen, Y. Sharma, L. Gresele, W. Brendel, B. Scholkopf, M. Besserve, and F. Locatello. Self-supervised learning with data augmentations provably isolates content from style. In *Advances in Neural Information Processing Systems*, 2021.

Kun Wang, Sumanth Varambally, Duncan Watson-Parris, Yian Ma, and Rose Yu. Discovering latent causal graphs from spatiotemporal data. In *Forty-second International Conference on Machine Learning*, 2025.

Ning Wang and Jin-Luen Lee. Geometric properties of the icosahedral-hexagonal grid on the two-sphere. *SIAM Journal on Scientific Computing*, 33(5):2536–2559, 2011.

T. Wiedemer, J. Brady, A. Panfilov, A. Juhos, M. Bethge, and W. Brendel. Provable compositional generalization for object-centric learning. In *International Conference on Learning Representations*, 2024.

Feng Xie, Yan Zeng, Zhengming Chen, Yangbo He, Zhi Geng, and Kun Zhang. Causal discovery of 1-factor measurement models in linear latent variable models with arbitrary noise distributions. *Neurocomputing*, 2023.

W. Yao, Y. Sun, A. Ho, C. Sun, and K. Zhang. Learning temporally causal latent processes from general temporal data. In *International Conference on Learning Representations*, 2022a.

Weiran Yao, Guangyi Chen, and Kun Zhang. Temporally disentangled representation learning. *arXiv preprint arXiv:2210.13647*, 2022b.

BT Thomas Yeo, Fenna M Krienen, Jorge Sepulcre, Mert R Sabuncu, Danial Lashkari, Marisa Hollinshead, Joshua L Roffman, Jordan W Smoller, Lilla Zöllei, Jonathan R Polimeni, et al. The organization of the human cerebral cortex estimated by intrinsic functional connectivity. *Journal of neurophysiology*, 2011.

K. Zhang, J. Peters, D. Janzing, and B. Schölkopf. Kernel-based conditional independence test and application in causal discovery. *Proceedings of the Twenty-Seventh Conference on Uncertainty in Artificial Intelligence*, 2011.

Qinyi Zhang, Sarah Filippi, Arthur Gretton, and Dino Sejdinovic. Large-scale kernel methods for independence testing. *Statistics and Computing*, 28:113–130, 2018.

Xun Zheng, Bryon Aragam, Pradeep K Ravikumar, and Eric P Xing. Dags with no tears: Continuous optimization for structure learning. *Advances in Neural Information Processing Systems*, 31, 2018.

Yujia Zheng, Ignavier Ng, and Kun Zhang. On the identifiability of nonlinear ica: Sparsity and beyond. *arXiv preprint arXiv:2206.07751*, 2022.

Dong Zhou, Avi Gozolchiani, Yosef Ashkenazy, and Shlomo Havlin. Teleconnection paths via climate network direct link detection. *Physical review letters*, 115(26):268501, 2015.

## Appendix A. Derivation of the ELBO

We show explicitly the derivation of the ELBO by starting from the marginal likelihood and by using the model we have proposed in Section 3.1.

$$\log p(\boldsymbol{x}^{\leq T}) = \mathbb{E}_{\boldsymbol{z}^{\leq T}\sim q(\boldsymbol{z}^{\leq T}|\boldsymbol{x}^{\leq T})}\left[\log p(\boldsymbol{x}^{\leq T})\frac{p(\boldsymbol{x}^{\leq T},\boldsymbol{z}^{\leq T})}{p(\boldsymbol{x}^{\leq T},\boldsymbol{z}^{\leq T})}\frac{q(\boldsymbol{z}^{\leq T}\mid\boldsymbol{x}^{\leq T})}{q(\boldsymbol{z}^{\leq T}\mid\boldsymbol{x}^{\leq T})}\right] \tag{9}$$

$$= \mathbb{E}_{\boldsymbol{z}^{\leq T}\sim q(\boldsymbol{z}^{\leq T}|\boldsymbol{x}^{\leq T})}\left[\log\frac{q(\boldsymbol{z}^{\leq T}\mid\boldsymbol{x}^{\leq T})}{p(\boldsymbol{z}^{\leq T}\mid\boldsymbol{x}^{\leq T})} + \log\frac{p(\boldsymbol{x}^{\leq T},\boldsymbol{z}^{\leq T})}{q(\boldsymbol{z}^{\leq T}\mid\boldsymbol{x}^{\leq T})}\right] \tag{10}$$

$$= \mathrm{KL}(q(\boldsymbol{z}^{\leq T}\mid\boldsymbol{x}^{\leq T})||p(\boldsymbol{z}^{\leq T}\mid\boldsymbol{x}^{\leq T})) + \mathbb{E}_{\boldsymbol{z}^{\leq T}\sim q(\boldsymbol{z}^{\leq T}|\boldsymbol{x}^{\leq T})}\left[\log\frac{p(\boldsymbol{x}^{\leq T},\boldsymbol{z}^{\leq T})}{q(\boldsymbol{z}^{\leq T}\mid\boldsymbol{x}^{\leq T})}\right]. \tag{11}$$

Since $\mathrm{KL}\geq 0$, we have:

$$\log p(\boldsymbol{x}^{\leq T}) \geq \mathbb{E}_{\boldsymbol{z}^{\leq T}\sim q(\boldsymbol{z}^{\leq T}|\boldsymbol{x}^{\leq T})}\left[\log\frac{p(\boldsymbol{x}^{\leq T},\boldsymbol{z}^{\leq T})}{q(\boldsymbol{z}^{\leq T}\mid\boldsymbol{x}^{\leq T})}\right]. \tag{12}$$

Now we will replace $p(\boldsymbol{x}^{\leq T},\boldsymbol{z}^{\leq T})$ and $q(\boldsymbol{z}^{\leq T}\mid\boldsymbol{x}^{\leq T})$ by the factorisation we assumed in Equation 4 and 5:

$$\log p(\boldsymbol{x}^{\leq T}) \geq \mathbb{E}_{\boldsymbol{z}^{\leq T}\sim q(\boldsymbol{z}^{\leq T}|\boldsymbol{x}^{\leq T})}\left[\log\frac{\prod_{t=1}^{T}p(\boldsymbol{z}^t\mid\boldsymbol{z}^{<t})p(\boldsymbol{x}^t\mid\boldsymbol{z}^t)}{\prod_{t=1}^{T}q(\boldsymbol{z}^t\mid\boldsymbol{x}^t)}\right] \tag{13}$$

$$\geq \mathbb{E}_{\boldsymbol{z}^{\leq T}\sim q(\boldsymbol{z}^{\leq T}|\boldsymbol{x}^{\leq T})}\left[\sum_{t=1}^{T}\log p(\boldsymbol{x}^t\mid\boldsymbol{z}^t)\right] + \mathbb{E}_{\boldsymbol{z}^{\leq T}\sim q(\boldsymbol{z}^{\leq T}|\boldsymbol{x}^{\leq T})}\left[\sum_{t=1}^{T}\log\frac{p(\boldsymbol{z}^t\mid\boldsymbol{z}^{<t})}{q(\boldsymbol{z}^t\mid\boldsymbol{x}^t)}\right]. \tag{14}$$

Finally, thanks to the decomposition of our proposed posterior (Equation 5), we have:

$$\log p(\boldsymbol{x}^{\leq T}) \geq \sum_{t=1}^{T}\Big[\mathbb{E}_{\boldsymbol{z}^t\sim q(\boldsymbol{z}^t|\boldsymbol{x}^t)}\left[\log p(\boldsymbol{x}^t\mid\boldsymbol{z}^t)\right] - \tag{15}$$

$$\mathbb{E}_{\boldsymbol{z}^{<t}\sim q(\boldsymbol{z}^{<t}|\boldsymbol{x}^{<t})}\mathrm{KL}\left[q(\boldsymbol{z}^t\mid\boldsymbol{x}^t)\,||\,p(\boldsymbol{z}^t\mid\boldsymbol{z}^{<t})\right]\Big]. \tag{16}$$

## Appendix B. Identifiability

In what follows, we overload the notation by defining $\boldsymbol{f}(\boldsymbol{z}^{\leq T}) := [\boldsymbol{f}(\boldsymbol{z}^1)\dots\boldsymbol{f}(\boldsymbol{z}^T)]$ and similarly for other functions.

**Lemma 3 (Denoising $\boldsymbol{x}$)** *Assume we have two models $p(\boldsymbol{x}^{\leq T},\boldsymbol{z}^{\leq T})$ and $\hat{p}(\boldsymbol{x}^{\leq T},\hat{\boldsymbol{z}}^{\leq T})$ as specified in Section 3.1 with parameters $(\boldsymbol{g},\boldsymbol{f},G,\sigma^2)$ and $(\hat{\boldsymbol{g}},\hat{\boldsymbol{f}},\hat{G},\hat{\sigma}^2)$, respectively. Assume $d_z < d_x$. Therefore, whenever $\int p(\boldsymbol{x}^{\leq T},\boldsymbol{z}^{\leq T})d\boldsymbol{z}^{\leq T} = \int\hat{p}(\boldsymbol{x}^{\leq T},\hat{\boldsymbol{z}}^{\leq T})d\hat{\boldsymbol{z}}^{\leq T}$ for all $\boldsymbol{x}^{\leq T}$, we have that the distributions of $\boldsymbol{y}^{\leq T} := \boldsymbol{f}(\boldsymbol{z}^{\leq T})$ and $\hat{\boldsymbol{y}}^{\leq T} := \hat{\boldsymbol{f}}(\hat{\boldsymbol{z}}^{\leq T})$ are equal.*

**Proof** Let $\mathbb{P}_{\boldsymbol{x}^{\leq T}}$ and $\mathbb{P}_{\hat{\boldsymbol{x}}^{\leq T}}$ be the probability measures respectively induced by the densities $p(\boldsymbol{x}^{\leq T}) := \int p(\boldsymbol{x}^{\leq T}, \boldsymbol{z}^{\leq T}) d\boldsymbol{z}^{\leq T}$ and $\hat{p}(\hat{\boldsymbol{x}}^{\leq T}) := \int \hat{p}(\hat{\boldsymbol{x}}^{\leq T}, \hat{\boldsymbol{z}}^{\leq T}) d\hat{\boldsymbol{z}}^{\leq T}$. We can thus write

$$\mathbb{P}_{\boldsymbol{x}^{\leq T}} = \mathbb{P}_{\hat{\boldsymbol{x}}^{\leq T}} \,. \tag{17}$$

Let us define $\boldsymbol{y}^t := \boldsymbol{f}(\boldsymbol{z}^t)$ and $\hat{\boldsymbol{y}}^t := \hat{\boldsymbol{f}}(\hat{z}^t)$ for all $t$ where $\boldsymbol{z}^{\leq T} \sim p(\boldsymbol{z}^{\leq T})$ and $\hat{\boldsymbol{z}}^{\leq T} \sim \hat{p}(\hat{\boldsymbol{z}}^{\leq T})$. Let $\mathbb{P}_{\boldsymbol{y}^{\leq T}}$ and $\mathbb{P}_{\hat{\boldsymbol{y}}^{\leq T}}$ be the probability distributions of $\boldsymbol{y}^{\leq T}$ and $\hat{\boldsymbol{y}}^{\leq T}$, respectively. Notice how we can write $\boldsymbol{x}^{\leq T} = \boldsymbol{y}^{\leq T} + \boldsymbol{n}^{\leq T}$ and $\hat{\boldsymbol{x}}^{\leq T} = \hat{\boldsymbol{y}}^{\leq T} + \hat{\boldsymbol{n}}^{\leq T}$, where $\boldsymbol{n}^t \sim \mathcal{N}(0, \sigma^2 I_{d_x})$ and $\hat{\boldsymbol{n}}^t \sim \mathcal{N}(0, \hat{\sigma}^2 I_{d_x})$ for all $t \leq T$, where the noises are mutually independent across time. This means we can write

$$\mathbb{P}_{\boldsymbol{y}^{\leq T}} * \mathbb{P}_{\boldsymbol{n}^{\leq T}} = \mathbb{P}_{\hat{\boldsymbol{y}}^{\leq T}} * \mathbb{P}_{\hat{\boldsymbol{n}}^{\leq T}} \,, \tag{18}$$

where $\mathbb{P}_{\boldsymbol{n}^{\leq T}}$ stands for the probability measure of the Gaussian noise (similarly for $\mathbb{P}_{\hat{\boldsymbol{n}}^{\leq T}}$) and $*$ stands for the convolution operator on measures.

The following step makes use of the Fourier transform $\mathcal{F}$ generalized to arbitrary probability measures. See Pollard (2001, Chapter 8). Note that the Fourier transform of a probability distribution is exactly the *characteristic function* of the random variable it represents.

$$\mathcal{F}(\mathbb{P}_{\boldsymbol{y}^{\leq T}} * \mathbb{P}_{\boldsymbol{n}^{\leq T}}) = \mathcal{F}(\mathbb{P}_{\hat{\boldsymbol{y}}^{\leq T}} * \mathbb{P}_{\hat{\boldsymbol{n}}^{\leq T}}) \tag{19}$$

$$\mathcal{F}(\mathbb{P}_{\boldsymbol{y}^{\leq T}}) \mathcal{F}(\mathbb{P}_{\boldsymbol{n}^{\leq T}}) = \mathcal{F}(\mathbb{P}_{\hat{\boldsymbol{y}}^{\leq T}}) \mathcal{F}(\mathbb{P}_{\hat{\boldsymbol{n}}^{\leq T}}) \tag{20}$$

$$\mathcal{F}(\mathbb{P}_{\boldsymbol{y}^{\leq T}})(\omega) e^{-\frac{\sigma^2}{2}\omega^\top \omega} = \mathcal{F}(\mathbb{P}_{\hat{\boldsymbol{y}}^{\leq T}})(\omega) e^{-\frac{\hat{\sigma}^2}{2}\omega^\top \omega} \,, \forall \omega \in \mathbb{R}^{T \cdot d_x} \,, \tag{21}$$

where we used the fact that (i) the Fourier transform of a convolution is the product of the Fourier transforms and (ii) the fact that the Fourier transform of a Gaussian random vector with mean 0 and covariance $\sigma^2 I$ is $e^{-\frac{\sigma^2}{2}\omega^\top \omega}$.

Now our goal is to show that $\sigma^2 = \hat{\sigma}^2$. Assume this is false, i.e. $\sigma^2 < \hat{\sigma}^2$ (w.l.o.g.). Because this Fourier transform is positive for all $\omega \in \mathbb{R}^{T \cdot d_x}$, we can divide by its value on both sides and obtain

$$\mathcal{F}(\mathbb{P}_{\boldsymbol{y}^{\leq T}})(\omega) = \mathcal{F}(\mathbb{P}_{\hat{\boldsymbol{y}}^{\leq T}})(\omega) e^{-\frac{\hat{\sigma}^2 - \sigma^2}{2}\omega^\top \omega} \,, \forall \omega \in \mathbb{R}^{T \cdot d_x} \,, \tag{22}$$

where we recognize that $e^{-\frac{\hat{\sigma}^2 - \sigma^2}{2}\omega^\top \omega}$ is the Fourier transform of a Gaussian distribution with mean zero and covariance $(\hat{\sigma}^2 - \sigma^2) I_{T \cdot d_x}$. Now notice how the l.h.s. is the Fourier transform of a distribution with support contained in $\boldsymbol{f}(\mathbb{R}^{T d_z})$, which is a $d_z$-dimensional manifold embedded in $\mathbb{R}^{T d_x}$. Since we assume $d_z < d_x$, the set $\boldsymbol{f}(\mathbb{R}^{T d_z})$ is a proper subset of $\mathbb{R}^{T d_x}$ (i.e. $\boldsymbol{f}(\mathbb{R}^{T d_z}) \neq \mathbb{R}^{T d_x}$). In contrast, the r.h.s. is the Fourier transform of a distribution with full support, i.e. $\mathbb{R}^{T d_x}$, since it is the convolution of $\mathbb{P}_{\hat{y}^{\leq T}}$ and a Gaussian distribution. This is a contradiction since both supports should be equal. Hence we must have that $\sigma^2 = \hat{\sigma}^2$. We can thus write

$$\mathcal{F}(\mathbb{P}_{\boldsymbol{y}^{\leq T}}) = \mathcal{F}(\mathbb{P}_{\hat{\boldsymbol{y}}^{\leq T}}) \tag{23}$$

$$\mathbb{P}_{\boldsymbol{y}^{\leq T}} = \mathbb{P}_{\hat{\boldsymbol{y}}^{\leq T}} \,, \tag{24}$$

which concludes the proof. ■

**Proposition 4 (Identifiability of $\boldsymbol{f}$ and $p(\boldsymbol{z}^{\leq T})$ up to diffeomorphism)** *Assume we have two models $p(\boldsymbol{x}^{\leq T}, \boldsymbol{z}^{\leq T})$ and $\hat{p}(\boldsymbol{x}^{\leq T}, \hat{\boldsymbol{z}}^{\leq T})$ as specified in Section 3.1 with parameters $(\boldsymbol{g}, \boldsymbol{f}, G, \sigma^2)$ and $(\hat{\boldsymbol{g}}, \hat{\boldsymbol{f}}, \hat{G}, \hat{\sigma}^2)$, respectively. Assume further that $\boldsymbol{f}$ and $\hat{\boldsymbol{f}}$ are diffeomorphisms onto their respective images and that $d_z < d_x$ (we do not assume single-parent decoding). Therefore, whenever $\int p(\boldsymbol{x}^{\leq T}, \boldsymbol{z}^{\leq T}) d\boldsymbol{z}^{\leq T} = \int \hat{p}(\boldsymbol{x}^{\leq T}, \hat{\boldsymbol{z}}^{\leq T}) d\hat{\boldsymbol{z}}^{\leq T}$ for all $\boldsymbol{x}^{\leq T}$, we have $\boldsymbol{f}(\mathbb{R}^{d_z}) = \hat{\boldsymbol{f}}(\mathbb{R}^{d_z})$ and $\boldsymbol{v} := \boldsymbol{f}^{-1} \circ \hat{\boldsymbol{f}}$ is a diffeomorphism. Moreover, the density of the ground-truth latents $p(\boldsymbol{z}^{\leq T})$ and the density of the learned latents $\hat{p}(\hat{\boldsymbol{z}}^{\leq T})$ are related via*

$$p(\boldsymbol{v}(\hat{\boldsymbol{z}}^{\leq T})) \prod_{t=1}^{T} |\det D\boldsymbol{v}(\hat{\boldsymbol{z}}^{t})| = \hat{p}(\hat{\boldsymbol{z}}^{\leq T}), \ \forall \hat{\boldsymbol{z}}^{\leq T} \in \mathbb{R}^{d_z \times T} .$$

**Proof** By Lemma 3, we have that

$$\mathbb{P}_{\boldsymbol{y}^{\leq T}} = \mathbb{P}_{\hat{\boldsymbol{y}}^{\leq T}} . \tag{25}$$

By marginalizing out $\boldsymbol{y}^{2:T}$ on both sides, we get

$$\mathbb{P}_{\boldsymbol{y}^{1}} = \mathbb{P}_{\hat{\boldsymbol{y}}^{1}} , \tag{26}$$

which of course implies that their supports are equal:

$$\text{supp}(\mathbb{P}_{\boldsymbol{y}^{1}}) = \text{supp}(\mathbb{P}_{\hat{\boldsymbol{y}}^{1}}) \tag{27}$$

$$\boldsymbol{f}(\text{supp}(p(\boldsymbol{z}^{t}))) = \hat{\boldsymbol{f}}(\text{supp}(\hat{p}(\hat{\boldsymbol{z}}^{t}))) \tag{28}$$

$$\boldsymbol{f}(\mathbb{R}^{d_z}) = \hat{\boldsymbol{f}}(\mathbb{R}^{d_z}) , \tag{29}$$

where $\text{supp}(\cdot)$ stands for support of a distribution. Note that the last step is because $p(z^1)$ is assumed to have full support (Section Section 3.1).

Equation (29) and the fact that both $\boldsymbol{f}$ and $\hat{\boldsymbol{f}}$ are diffeomorphisms onto their image implies that the map $\boldsymbol{v} := \boldsymbol{f}^{-1} \circ \hat{\boldsymbol{f}}$ is both well-defined and a diffeomorphism.

From (25), we get

$$\mathbb{P}_{\boldsymbol{z}^{\leq T}} \circ \boldsymbol{f}^{-1} = \mathbb{P}_{\hat{\boldsymbol{z}}^{\leq T}} \circ \hat{\boldsymbol{f}} \tag{30}$$

$$\mathbb{P}_{\boldsymbol{z}^{\leq T}} \circ \boldsymbol{f}^{-1} \circ \hat{\boldsymbol{f}} = \mathbb{P}_{\hat{\boldsymbol{z}}^{\leq T}} \tag{31}$$

$$\mathbb{P}_{\boldsymbol{z}^{\leq T}} \circ \boldsymbol{v} = \mathbb{P}_{\hat{\boldsymbol{z}}^{\leq T}} . \tag{32}$$

The above equation combined with the change-of-variable formula yields

$$p(\boldsymbol{v}(\hat{\boldsymbol{z}}^{\leq T})) \prod_{t=1}^{T} |\det D\boldsymbol{v}(\hat{\boldsymbol{z}}^{t})| = \hat{p}(\hat{\boldsymbol{z}}^{\leq T}), \ \forall \hat{\boldsymbol{z}}^{\leq T} \in \mathbb{R}^{d_z \times T} , \tag{33}$$

which concludes the proof. ■

**Proposition 5 (Identifying latents of $\boldsymbol{f}$)** *Let $\boldsymbol{f} : \mathbb{R}^{d_z} \to \mathbb{R}^{d_x}$ and $\hat{\boldsymbol{f}} : \mathbb{R}^{d_z} \to \mathbb{R}^{d_x}$ be two diffeomorphisms onto their image $\boldsymbol{f}(\mathbb{R}^{d_z}) = \hat{\boldsymbol{f}}(\mathbb{R}^{d_z})$. Assume both $\boldsymbol{f}$ and $\hat{\boldsymbol{f}}$ have a single-parent decoding structure, i.e. $|pa_j^F| \leq 1$ and $|pa_j^{\hat{F}}| \leq 1$. Then, the map $\boldsymbol{v} := \boldsymbol{f}^{-1} \circ \hat{\boldsymbol{f}}$ has the following property: there exists a permutation $\pi$ such that, for all $i$, the function $\boldsymbol{v}_i(\boldsymbol{z})$ depends only on $\boldsymbol{z}_{\pi(i)}$.*

**Proof** We see that $\boldsymbol{v} = \boldsymbol{f}^{-1} \circ \hat{\boldsymbol{f}}$ implies

$$\hat{\boldsymbol{f}} = \boldsymbol{f} \circ \boldsymbol{v}\,. \tag{34}$$

Taking the derivative on both sides of Equation 34, write

$$D\hat{\boldsymbol{f}}(\boldsymbol{z}) = D(\boldsymbol{f} \circ \boldsymbol{v})(\boldsymbol{z}) = D\boldsymbol{f}(\boldsymbol{v}(\boldsymbol{z}))D\boldsymbol{v}(\boldsymbol{z}), \tag{35}$$

where the second equality follows from applying the chain rule, each Jacobian $D\hat{\boldsymbol{f}}(\boldsymbol{z})$ and $D\boldsymbol{f}(\boldsymbol{v}(\boldsymbol{z}))$ is a $d_x \times d_z$ matrix and the Jacobian $D\boldsymbol{v}(\boldsymbol{z})$ is a $d_z \times d_z$ matrix.

In words, Equation 34 tells us that the mapping $\hat{\boldsymbol{f}}$ is "imitating" the mapping $\boldsymbol{f}$ in the following sense: Evaluating $\hat{\boldsymbol{f}}$ is the same as first evaluating $\boldsymbol{v}$ and then evaluating $\boldsymbol{f}$.

We need to show that $\boldsymbol{v}(\boldsymbol{z})$ is a permutation-scaling transformation in the sense defined in the statement of this proposition. To achieve this, we will show that the Jacobian $D\boldsymbol{v}(\boldsymbol{z})$ is a permutation-scaling matrix for all $\boldsymbol{z}$.

We show this in a number of steps:

**Step 1.** Since $\hat{\boldsymbol{f}}$ is a diffeomorphism, its Jacobian, $D\hat{\boldsymbol{f}}$, has full column rank everywhere. Thus, its Moore-Penrose inverse (also known as its pseudo-inverse), $D\hat{\boldsymbol{f}}(\boldsymbol{z})^+$, can be written as,

$$D\hat{\boldsymbol{f}}(\boldsymbol{z})^+ = (D\hat{\boldsymbol{f}}(\boldsymbol{z})^\top D\hat{\boldsymbol{f}}(\boldsymbol{z}))^{-1} D\boldsymbol{f}(\boldsymbol{z})^\top. \tag{36}$$

Further, $D\hat{\boldsymbol{f}}(\boldsymbol{z})^+$ is a left inverse; that is, $D\hat{\boldsymbol{f}}(\boldsymbol{z})^+ D\hat{\boldsymbol{f}}(\boldsymbol{z}) = I$.

We can left-multiply both sides of Equation 35 by $D\hat{\boldsymbol{f}}(\boldsymbol{z})^+$, yielding,

$$I = (D\hat{\boldsymbol{f}}(\boldsymbol{z})^\top D\hat{\boldsymbol{f}}(\boldsymbol{z}))^{-1} D\hat{\boldsymbol{f}}(\boldsymbol{z})^\top D\boldsymbol{f}(\boldsymbol{v}(\boldsymbol{z}))D\boldsymbol{v}(\boldsymbol{z}). \tag{37}$$

**Step 2.** We now show that the matrix $D\hat{\boldsymbol{f}}(\boldsymbol{z})^\top D\hat{\boldsymbol{f}}(\boldsymbol{z})$ is diagonal. To see this, consider $k \neq k'$ and write

$$(D\hat{\boldsymbol{f}}(\boldsymbol{z})^\top D\hat{\boldsymbol{f}}(\boldsymbol{z}))_{k,k'} = \sum_{d=1}^{d_x} D\hat{\boldsymbol{f}}(\boldsymbol{z})_{d,k} D\hat{\boldsymbol{f}}(\boldsymbol{z})_{d,k'}. \tag{38}$$

This must be zero since, otherwise, it would imply that there exists a $d$ such that both $D\hat{\boldsymbol{f}}(\boldsymbol{z})_{d,k}$ and $D\hat{\boldsymbol{f}}(\boldsymbol{z})_{d,k'}$ are different from zero, but this is impossible since $y_d$ has only one parent in the graph $F$ (by the "single-parent property").

Define $\Lambda(\boldsymbol{z}) := D\hat{\boldsymbol{f}}(\boldsymbol{z})^\top D\hat{\boldsymbol{f}}(\boldsymbol{z})$, which we just showed is diagonal. Equation 37 implies that

$$D\boldsymbol{v}(\boldsymbol{z})^{-1} = \Lambda(\boldsymbol{z})^{-1} D\hat{\boldsymbol{f}}(\boldsymbol{z})^\top D\boldsymbol{f}(\boldsymbol{v}(\boldsymbol{z})), \tag{39}$$

and since $D\boldsymbol{v}(\boldsymbol{z})^{-1}$ is invertible, $D\hat{\boldsymbol{f}}(\boldsymbol{z})^\top D\boldsymbol{f}(\boldsymbol{v}(\boldsymbol{z}))$ must also be invertible.

**Key idea.** To show that $D\boldsymbol{v}(\boldsymbol{z})$ is a permutation-scaling matrix, we will show that its inverse is a permutation-scaling matrix. We have already shown that $\Lambda(\boldsymbol{z})$ is a diagonal matrix. Thus, what remains is to show that $D\hat{\boldsymbol{f}}(\boldsymbol{z})^\top D\boldsymbol{f}(\boldsymbol{v}(\boldsymbol{z}))$ is a permutation-scaling matrix.

**Step 3.** For any $d_z \times d_z$ invertible matrix $L$,

$$\det(L) = \sum_{\pi \in \Pi_{d_z}} \operatorname{sign}(\pi) \prod_{k=1}^{d_z} L_{\pi(k),k} \neq 0,$$

where $\Pi_{d_z}$ is the set of $(d_z)$-permutations. This implies that there exists a permutation $\pi \in \Pi_{d_z}$ so that for all $k \leq d_z$, $L_{\pi(k),k} \neq 0$.

Applying this result to the invertible matrix $D\hat{\boldsymbol{f}}(\boldsymbol{z})^\top D\boldsymbol{f}(\boldsymbol{v}(\boldsymbol{z}))$,

$$\begin{aligned} &\exists \pi \in \Pi_{d_z} : \forall k \leq d_z, (D\hat{\boldsymbol{f}}(\boldsymbol{z})^\top D\boldsymbol{f}(\boldsymbol{v}(\boldsymbol{z})))_{\pi(k),k} \neq 0 \\ &\implies \forall k \leq d_z, \sum_{d=1}^{d_x} D\hat{\boldsymbol{f}}(\boldsymbol{z})_{d,\pi(k)} D\boldsymbol{f}(\boldsymbol{v}(\boldsymbol{z}))_{d,k} \neq 0 \\ &\implies \forall k \leq d_z, \ \exists d_1 : D\hat{\boldsymbol{f}}(\boldsymbol{z})_{d_1.\pi(k)} \neq 0 \neq D\boldsymbol{f}(\boldsymbol{v}(\boldsymbol{z}))_{d_1,k}. \end{aligned} \tag{40}$$

**Key idea.** To show that $D\hat{\boldsymbol{f}}(\boldsymbol{z})^\top D\boldsymbol{f}(\boldsymbol{v}(\boldsymbol{z}))$ is a permutation-scaling matrix, we want to show that this matrix has nonzero values *only* at entries of the form $(\pi(k), k)$. We will prove this by contradiction, using the existence of the observed feature $y_{d_1}$ from Equation 40.

**Step 4.** By contradiction, suppose there exists a pair of indices $(k, k')$ such that $k' \neq \pi(k)$ and

$$(D\hat{\boldsymbol{f}}(\boldsymbol{z})^\top D\boldsymbol{f}(v(\boldsymbol{z})))_{k',k} = \sum_{d=1}^{d_x} D\hat{\boldsymbol{f}}(\boldsymbol{z})_{k',d}^\top D\boldsymbol{f}(\boldsymbol{v}(\boldsymbol{z}))_{d,k} \neq 0\,. \tag{41}$$

This means that there exists a feature $y_{d_2}$ so that

$$D\hat{\boldsymbol{f}}(\boldsymbol{z})_{d_2,k'} \neq 0 \neq D\boldsymbol{f}(\boldsymbol{v}(\boldsymbol{z}))_{d_2,k}\,. \tag{42}$$

We know that $d_2$ is not equal to $d_1$ from Equation 40, since if $d_1$ and $d_2$ were the same index, then $y_{d_1}$ would have two distinct parents if $\hat{\boldsymbol{f}}$, namely $\pi(k)$ and $k'$ .

By selecting only rows $d_1$ and $d_2$ in Equation 35, we obtain the following equality

$$D\hat{\boldsymbol{f}}(\boldsymbol{z})_{\{d_1,d_2\},\cdot} = D\boldsymbol{f}(\boldsymbol{v}(\boldsymbol{z}))_{\{d_1,d_2\},\cdot} D\boldsymbol{v}(\boldsymbol{z}). \tag{43}$$

By (40) & (42) and the fact that both $\boldsymbol{f}$ and $\hat{\boldsymbol{f}}$ satisfy the "single-parent property", we have

$$D\hat{\boldsymbol{f}}(\boldsymbol{z})_{\{d_1,d_2\},\cdot} = \begin{array}{c} \\ d_1 \\ d_2 \end{array} \begin{array}{c} \begin{array}{cccccccc} & & & & \pi(k) & k' & & \end{array} \\ \begin{pmatrix} 0 & \cdots & 0 & * & 0 & 0 & \cdots & 0 \\ 0 & \cdots & 0 & 0 & * & 0 & \cdots & 0 \end{pmatrix} \end{array} \tag{44}$$

$$D\boldsymbol{f}(\boldsymbol{v}(\boldsymbol{z}))_{\{d_1,d_2\},\cdot} = \begin{array}{c} \\ d_1 \\ d_2 \end{array} \begin{array}{c} \begin{array}{ccccccc} & & & k & & & \end{array} \\ \begin{pmatrix} 0 & \cdots & 0 & * & 0 & \cdots & 0 \\ 0 & \cdots & 0 & * & 0 & \cdots & 0 \end{pmatrix} \end{array}, \tag{45}$$

where $*$ denotes nonzero entries. From the above, it is clear that $D\hat{\boldsymbol{f}}(\boldsymbol{z})_{\{d_1,d_2\},\cdot}$ has a rank of 2 and $D\boldsymbol{f}(\boldsymbol{v}(\boldsymbol{z}))_{\{d_1,d_2\},\cdot}$ has a rank of 1. Since $D\boldsymbol{v}(\boldsymbol{z})$ is invertible we have that the r.h.s. of (43) has rank 1. Equation (43) is thus a contradiction since the l.h.s. has rank 2.

Thus, $(D\hat{\boldsymbol{f}}(\boldsymbol{z})^\top D\boldsymbol{f}(\boldsymbol{v}(\boldsymbol{z})))_{k',k} \neq 0$ if and only if $k' = \pi(k)$, where $\pi$ is a $(d_z)$-permutation. In other words, $D\hat{\boldsymbol{f}}(\boldsymbol{z})^\top D\boldsymbol{f}(\boldsymbol{v}(\boldsymbol{z}))$ is a permutation-scaling matrix.

Going back to Equation 39, $D\boldsymbol{v}(\boldsymbol{z})^{-1}$ is a permutation-scaling matrix since it is a product of a diagonal matrix and a permutation-scaling matrix. Thus, its inverse, $D\boldsymbol{v}(\boldsymbol{z})$, is also a permutation-scaling matrix.

The argument above holds *point-wise*, i.e. for each $\boldsymbol{z}$. However, *a priori*, it is possible that the permutation $\pi$ changes for different values of $\boldsymbol{z}$. It turns out this is impossible since that would violate the fact that $D\boldsymbol{v}(\boldsymbol{z})$ is continuous. ■

## Appendix C. Optimization

### C.1. Augmented Lagrangian Method

The main idea of the Augmented Lagrangian Method (ALM) is to remove constraints in an optimization problem and instead add a penalty term to the objective (For more detailed explanations, see Nocedal and Wright (1999), Chapter 17). For an optimization problem where we aim to minimize $\mathcal{L}(x)$ subject to a constraint $h(\boldsymbol{x}) = 0$, the equivalent ALM objective is:

$$L(\boldsymbol{x}, \lambda_k, \mu_k) = \mathcal{L}(\boldsymbol{x}) + \lambda_k h(\boldsymbol{x}) + \frac{\mu_k}{2}||h(\boldsymbol{x})||^2.$$

To approximately solve the constrained problem, a sequence of problems will be solved where $\lambda_k$ and $\mu_k$ will be incrementally increased as $k$ increases. A problem is considered solved when the loss on a held-out dataset does not decrease. Then, a new problem is initialized with the values $\lambda_{k+1}$ and $\mu_{k+1}$:

$$\lambda_{k+1} \leftarrow \lambda_k + \mu_k \cdot h(W^*_{(k)})$$
$$\mu_{k+1} \leftarrow \begin{cases} \eta \cdot \mu_k, & \text{if } h(W^*_{(k)}) > \delta \cdot h(W^*_{(k-1)}) \\ \mu_k, & \text{otherwise} \end{cases}$$

where $\mu_k > 0$ and $\eta > 1$ and $W^*_{(k)}$ is the approximate solution to the $k$-th problem.

### C.2. Projected Gradient

The projected gradient descent method can be used when some parameters are under constraints. In general, we proceed in two steps: 1) perform a step of gradient descent and 2) project the result on the feasible set. More formally, we do a normal gradient descent step from $x_k$ :

$$y_{k+1} = x_k - \alpha \nabla f(x_k),$$

and then we project the result $y_{k+1}$ on the feasible set $\mathcal{Q}$:

$$x_{k+1} = \arg\min_{x \in \mathcal{Q}} \frac{1}{2}||x - y_{k+1}||_2^2.$$

In our case, the feasible set is $\mathbb{R}_{\geq 0}$, thus the projection is simply:

$$x_{k+1} = \begin{cases} y_{k+1} & \text{if } y_{k+1} \geq 0 \\ 0 & \text{otherwise.} \end{cases} \tag{46}$$

### C.3. Stochastic mask

For nonlinear mixing experiments, we obtained better performance by treating the mask $W$ as a stochastic variable, analogously to the latent graphs $G$. Concretely, we model $W$ as a random Bernoulli matrix $W \sim \text{Bernoulli}(\sigma(\tilde{W}))$ where $\tilde{W} \in \mathbb{R}^{d_x \times d_z}$ are the logits parameterizing the distribution. Under this parameterization, the optimization problem becomes:

$$\begin{aligned} &\max_{\tilde{W},\Gamma,\boldsymbol{\phi}} \mathbb{E}_{W\sim\sigma(\tilde{W})}\mathbb{E}_{G\sim\sigma(\Gamma)}\mathbb{E}_{\boldsymbol{x}}\left[\mathcal{L}_{\boldsymbol{x}}(\tilde{W},\Gamma,\boldsymbol{\phi})\right] - \lambda_s||\sigma(\Gamma)||_1 \\ &\text{s.t. } (\sigma(\tilde{W})^\top\sigma(\tilde{W}))_{ij} = 0, \quad \forall i \neq j \end{aligned} \tag{47}$$

As for the latent graphs $G$, we use the Gumbel-Softmax estimator to obtain gradients with respect to $\tilde{W}$. For the constraint, $\sigma(\tilde{W})$ is non-negative by construction, and we deliberately avoid enforcing the diagonal entries of $\sigma(\tilde{W})^\top\sigma(\tilde{W})$ to be exactly 1, as this would incentivize the model to push the Bernoulli parameters toward small values.

An alternative would be to enforce a one-hot structure applying a Softmax row-wise. While this approach enforces orthogonality automatically, we found in practice that it leads to substantially worse performance.

## Appendix D. Datasets

### D.1. Synthetic Datasets

Here, we detail the generative process of the synthetic datasets. The four main steps are:

1. Sample transition graphs $G \in \{0,1\}^{\tau\times d_z\times d_z}$.
2. Sample mechanisms to generate the latent variables $\boldsymbol{z}$ with relations following $G$.
3. Sample a matrix $W$.
4. Sample mechanisms of the decoding function to generate the observable $\boldsymbol{x}$ from $\boldsymbol{z}$.

**1- Graphs G**. For the adjacency matrices representing the lagged relations, we sampled independently $G^k_{ij} \sim Bernoulli(p)$ where $p \in [0,1]$ is a parameter corresponding to the probability of adding an edge. As a reminder: $G^k_{ij} = 1$ if and only if $z^{t-k}_j$ is a parent of $z^t_i$. Note that since these adjacency matrices represent links at different timesteps, we don't need to sample DAGs since it is impossible to create cycles.

For the graph $G^1$, we systematically set the elements of its diagonal to 1. These edges correspond to the relations of $z^t_i$ to themselves at the previous timestep: $z^{t-1}_i$. This assumption is often observed in real-world phenomena and is commonly used to generate time-series datasets (Runge et al., 2019b; Li and Genton, 2009).

**2- Dynamic's functions**. We first explain how we generate the mechanisms for the *nonlinear* case and, since it is a particular case, we then explain the *linear* case.

It is not obvious in general how to sample a nonlinear generative process that is stationary or, at least, that won't greatly diverge over time. In order to have non-divergent generative processes with nonlinear functions, we follow (Li and Genton, 2009) (See Theorem 1). Their method relies on two tricks: 1) the process is additive and the functions used have a linear behavior for large values, and 2) the coefficients are chosen so that an equivalent linear process would be stationary.

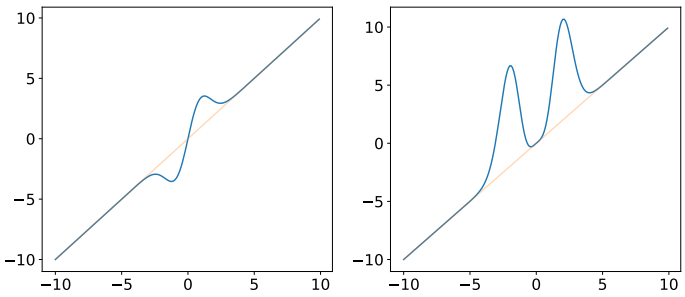


Figure 6: Examples of nonlinear functions used for the dynamics. For large values, the functions behave as linear functions.

We use the following structural equation:

$$z_i^t := \sum_{k=0}^{\tau} \sum_{j=1}^{d_z} G_{ij}^k A_{ij}^k s_{ij}^k(z_j^{t-k}) + \epsilon_i,$$

where $\epsilon_i \sim \mathcal{N}(0,1)$ and the coefficients $A_{ij}$ are independently sampled from $\mathcal{U}([-1,-0.2] \cup [0.2,1])$ and will be reweighted to ensure stationary. The range around 0 is removed to ensure that the data is faithful to the graph. Following (Runge et al., 2019b), each nonlinear dynamic's function $s_{ij}^k$ has a structure similar to:

$$f_1(x) = x(1 + 4e^{\frac{-x^2}{2}})$$

$$f_2(x) = x(1 + 4x^3 e^{\frac{-x^2}{2}}).$$

See the code to see all the functions that were used. As it can be noticed in Fig. 6, these functions are almost linear when $x$ is large. Then, to make the process stationary, we have to make sure that the linear process that has the same coefficient matrix $A$ would be stationary. One way to verify this is to make sure that all the eigenvalues of the following matrix $H$ have a modulus of less than one:

$$H = \begin{bmatrix} A^\tau & A^{\tau-1} & \dots & A^0 \\ I_\tau & 0 & \dots & 0 \\ 0 & \dots & 0 & \vdots \\ 0 & 0 & I_\tau & 0 \end{bmatrix} \tag{48}$$

To do so, we compute the spectrum $\rho(H)$ and we divide each matrix $A^k$ by $\rho(H)^{k+1}$. The resulting process will be stationary (Li and Genton, 2009).

For the *linear* datasets, we follow the same sampling process except that $s_{ij}^k$ is the identity.

**3- Graph F**. To generate the observable $\boldsymbol{x}$ from $\boldsymbol{z}$, we first sample the matrix $W \in \mathbb{R}_{\geq 0}^{d_x \times d_z}$ which is non-negative and orthogonal following these steps:

1. We first sample an assignment matrix $M \in \{0,1\}^{d_x \times d_z}$ where in each row, only one element is set to 1 and the rest is equal to 0. We also make sure that for each column, there is at least one element equal to 1.

2. We sample independently $A_{ij} \sim \mathcal{U}([0.2, 1])$ and mask it: $\tilde{W} := M \odot A$.

3. Finally, we normalize the column of $W$ to ensure that it is orthogonal. In other words: $W_{:j} := \frac{\tilde{W}_{:j}}{||\tilde{W}_{:j}||_2}$.

**4- Decoding functions.** In the nonlinear case, the function $r_j$ (from Section 3.3 §3) are given by functions of the forms:

$$f(x) = \sin\left(\frac{a + (a + b)x}{\pi}\right)$$

where $b = 2$ and $a$ varies for different children of a given $z$. In the linear case, each function $r_j$ is the identity. We sample the observable $\boldsymbol{x}$ following:

$$x_j^t \mid \boldsymbol{z}^t \sim \mathcal{N}(r_j(W\boldsymbol{z}^t), \sigma_j^2),$$

where $\sigma_j^2 = 0.1$ and $0.5$ in experiments with linear and nonlinear decoding, respectively.

### D.2. Real-world Datasets

Here, we describe how the sea-level pressure data was regridded to an icosahedral-hexagonal grid to achieve an equal-area projection (Majewski, 1998; Majewski et al., 2002). This form of regridding is motivated by the fact that the poles are singularities in the traditional longitude-latitude grid, i.e. that each grid cell contains a different amount of total surface area (for $1^\circ \times 1^\circ$ resolution, the length of a grid cell decreases from $\approx 111$ km at the equator to 0 km at the poles). This means that more grid cells represent a smaller area the further we move from the equator towards the south or north poles, leading to an overrepresentation of polar regions and an underrepresentation of equatorial regions. One way to address this issue is by projecting the data on a geodesic grid, such as the icosahedral-hexagonal grid (Sahr et al., 2003), as nowadays used in climate models (e.g. ICON, see Pham et al. (2021)). By regridding the data we can ensure that northern/southern weather regions are not overrepresented in the clustering and during the causal discovery process.

The sea-level pressure data was projected to the GME icosahedral grid (Majewski et al., 2002), with first-order conservative remapping (Jones, 1999) and the number of intervals $NI = 24$ to match the original resolution of $2.5^\circ \times 2.5^\circ$ at the equator as closely as possible. The original netCDF4 input files had to be converted to GRIB2 files for this purpose since netCDF4 files can only store quadrilateral data, whereas GRIB2 has no such restrictions (Dey et al., 2007). After making the original data GRIB2 compliant and converting it to this format, Climate Data Operators (CDO) (Schulzweida, 2022), was used to remap the longitude-latitude gridded data to the GME icosahedral-hexagonal grid. Two parameters are relevant during the regridding process: 1) $NI$, the number of intervals, and 2) the remapping function. The number of intervals was chosen in a manner to resemble the resolution of the original data at the equator, and in a manner to allow the recursive generation of bisected equilateral triangles (Wang and Lee, 2011). The remapping function was chosen to ensure a monotonic remapping that can deal with a fine-to-coarse setting. First-order or second-order conservative remapping seem to be the best choices for that and we decided to use first-order conservative remapping since it is sufficiently accurate and easier to handle. The regridded sea-level pressure files in GRIB2 format can be easily loaded with the xarray package in Python (Hoyer and Hamman, 2017).

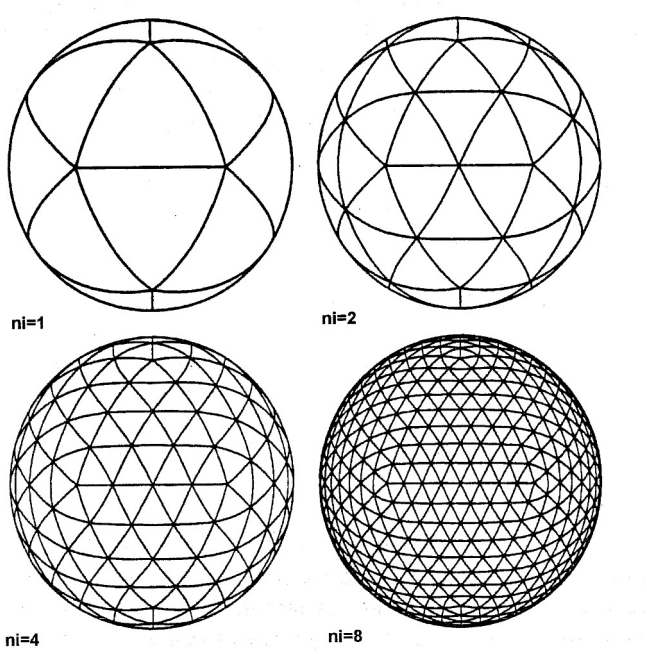


Figure 7: Visualization of icosahedral-hexagonal grids with different $NI$'s (number of intervals on triangle edge). the grid is generated recursively by halving the triangles, resulting in new, finer triangles. The figure stems from Majewski (1998).

## Appendix E. Methods and implementation details

### E.1. Varimax-PCMCI

Varimax-PCMCI is a two-step method where 1) a dimensionality reduction is conducted to obtain time series of latent variables and then 2) a causal discovery method is applied on the latent level time series. We follow Tibau et al. (2022) by using PCA with a Varimax-rotation as the dimensionality reduction method. This method was observed empirically in Tibau et al. (2022) to lead to better results. For more details on PCA-Varimax, see Appendix I. For the causal discovery algorithm we use PCMCI+ (Runge, 2020) which is an update to PCMCI, that also supports instantaneous connections. For the conditional independence tests used by PCMCI+, we use the partial correlation test for linear dynamics and the CMI-knn test (Runge, 2018), which is a test based on a nearest-neighbor estimator of conditional mutual information, for nonlinear dynamics. We use the implementation from `https://github.com/jakobrunge/tigramite` and `https://github.com/xtibau/savar/tree/master/savar`.

The significance level in PCMCI+ was set to $\alpha_{\mathrm{PC}} = 0.2$ and the time lags of causal links were restricted to $\tau \geq 1$, hence, only lagged links are considered. PCMCI+ then still slightly differs from PCMCI. Both share the $\mathrm{PC}_1$ phase that detects lagged (supersets) of parents, but they differ in the second phase because the MCI tests are only restricted to the superset of parents found in the first phase in PCMCI+ (Runge, 2020), whereas all lagged links are tested again in case of PCMCI.

### E.2. CDSD

For all neural networks, we use leaky-ReLU as activation functions. For the neural networks $g_j$ fitting the nonlinear dynamic, we used MLPs with 2 hidden layers and 8 hidden units. For the neural network $r_j$ fitting the nonlinear encoding, we use neural networks that receives as input the masked $W\boldsymbol{z}^t$. These neural networks have 2 hidden layers and 16 hidden units. The log of the variance terms and the matrix $W$ are free parameters initialized respectively to $-4$ and $\mathcal{U}[\frac{1}{10d_z}, \frac{1}{d_z}]$. The parameters $\Gamma$ are initialized to 5 which corresponds to an almost full graph (i.e. $\sigma(\Gamma) \approx \mathbf{1}$). We use the optimizer RMSProp (Hinton et al., 2012) with a learning rate of $1e-3$ and batch size of 64.

### E.3. MCC Metric

As stated in the main text, the mean coefficient correlation (MCC) is a metric commonly used in causal representation learning to assess the quality of the learned representation. It is necessary since the identifiability result is up to permutation. We use an implementation from Khemakhem et al. (2020a) (https://github.com/ilkhem/icebeem/blob/master/metrics/mcc.py). This corresponds to calculating the Pearson correlation between the learned representation $\hat{\boldsymbol{z}}$ and the ground-truth $\boldsymbol{z}$ under all possible permutations, selecting the permutation $\pi$ leading to the highest score, and taking its mean. To calculate the SHD between the learned graph $\hat{G}$ and $G$, we first apply the permutation $\pi$ to the learned graph.

## Appendix F. Hyperparameter Search

For all experimental conditions, we use the default hyperparameters specified in Table 1, 2 and 3. These values were determined based on the SHD from a few experiments on distinct synthetic datasets than those used for evaluation. The regularisation coefficient (for the graph sparsity of CDSD) and the alpha term (the significance threshold for the conditional independence tests of Varimax-PCMCI) have a bigger impact in terms of performance and accordingly they vary per dataset. For both methods, they have been tested respectively on the log scale $[-3, 1]$ and $[-11, -1]$. For these values, for each experimental condition, 10 datasets (distinct from evaluation) were used each with 10 different values of regularisation and alpha. The average of the parameter value leading to the best SHD of the 10 datasets was used for the synthetic experiments. As stated earlier, both $d_z$ and $\tau$ are given when using synthetic datasets. In the linear dynamics case, Varimax-PCMCI uses the partial correlation test and CDSD uses neural networks $g_j$ without hidden layers. In the nonlinear dynamics case, Varimax-PCMCI uses the CMI-knn test and CDSD uses neural networks $g_j$ with 2 hidden layers and 8 hidden units.

For the real-world dataset, we reused the same default hyperparameters. For the regularisation coefficient, we selected it based on the mean-square error between the prediction $\hat{\boldsymbol{x}}^t$ and $\boldsymbol{x}^t$ on a held-out testing set. The split ratio is 0.8 for the training set and 0.2 for the testing set.

## Appendix G. Additional experiments

### G.1. Running Time

We show the running time of CDSD and Varimax-PCMCI as a function of the number of samples and the number of latent variables. Note that the methods have not been highly optimized and that these running times are only given to give a general idea and assess the trends of growth. Varimax-PCMCI

Table 1: Default hyperparameters for CDSD with linear decoding

| CDSD hyperparameters |
|---|
| **ALM parameters**: |
| threshold: $10^{-4}$, $\mu_0$: $10^{-3}$, $\gamma_0$: 0, $\eta$: 2, $\delta$: 0.9 |
| **Optimizer**: |
| RMSProp, learning rate: $10^{-3}$, batch size: 64 |
| **Transition NN ($g_j$):** |
| Nonlinearity: Leaky-ReLU, |
| # hidden layers: [linear = 0, nonlinear = 2], |
| # hidden units: 8 |

Table 2: Default hyperparameters for CDSD with nonlinear decoding

| CDSD hyperparameters |
|---|
| **ALM parameters**: |
| $\mu_0$: $10^{-8}$, $\eta$: 1.5 |
| **Encoder/Decoder NN for nonlinear encoding:** |
| Nonlinearity: Leaky-ReLU, |
| # hidden layers: 2, hidden units: 16 |

is much faster than CDSD when using partial correlation as the conditional independence test (see the left panels of Fig. 8 and 9). However, for the nonlinear dynamics, CDSD is much faster, whereas Varimax-PCMCI often requires more than 24 hours to run. We only included cases where the time was under 24 hours (see the right panels of Fig. 8 and 9).

In Figure 8, it can be observed that for linear dynamics, the running time is almost constant in function of the number of samples. However, for the nonlinear dynamics, the time for Varimax-PCMCI increases steeply and is $>$ 24h for 5000 samples. In Figure 9, it can be observed that, as expected, the running time increases as the number of latent variables of the model increases. The same pattern can be observed for Varimax-PCMCI: while the running time is extremely low for linear functions, it is very high and only below 24 hours when 5 latent variables (with 5000 samples) are considered.

All experiments were run on AMD EPYC 7742 2.25GHz 64-Core Processor with 40G of RAM. We present in Table 4 the total running time for the main experiments.

### G.2. Statistical tests

Here we report the statistical tests comparing the performance of CDSD and Varimax-PCMCI for the results shown in Fig. 2 and Fig. 4. Since the high variability comes from the different datasets, we use a paired test: the Wilcoxon signed-rank test. We report the results in Appendix G.2 where the last two columns are the results of the Wilcoxon test. As stated in the text, all conditions are significantly different except when $d_z = 20$. Finally, for the ablation study, the result of the Wilcoxon signed-rank test is $W = 0; p = 0.001$.

Table 3: Default hyperparameters for PCMCI+

| PCMCI+ hyperparameters |
|---|
| $\alpha_{PC}$ = 0.2 |
| $\tau_{min} = 1$ |
| CI test: linear = partical corr., nonlinear = CMI-knn |

Table 4: Running time for each set of experiments

| Synthetic experiments |
|---|
| **Linear dynamics, linear decoder:** |
| CDSD: 76 hours |
| Varimax-PCMCI: 0.3 hours |
| **Nonlinear dynamics, linear decoder:** |
| CDSD: 116 hours |
| Varimax-PCMCI: 1212 hours |
| **Real-world experiments:** 75 hours |

### G.3. Synthetic Experiments

We show in Fig. 10 the results of CDSD on all the different experimental conditions in the nonlinear dynamics case. These results were not included in the main text since, as explained in the previous section, Varimax-PCMCI had a running time too high in most conditions. It can be observed that overall the nonlinear dynamics seems to be a more challenging task than its linear counterpart. Otherwise, the general trends are similar (improvement with the number of samples, deterioration as the other parameters increase).

### G.4. Real-world Experiment

In this section, we present additional results on the real-world dataset. Specifically, we show an alternative result using lower regularization, provide a clearer visualization of the learned clusters, and present further results with a lower number of latents.

In Fig. 11 we show an alternate result that had a similar validation loss, but learned a denser graph. Overall, the conclusions remain the same. It can be observed that the learned spatial aggregation is nearly identical to the one in the main text. The graph is denser, but the same general pattern is observed: $G^1$ is denser, the diagonal has edges, etc. Furthermore, a similar pattern can be observed between the nodes related to ENSO with two additional edges.

In the main text, we claimed that the learned clusters are localized. Since in the main figure of the real-world application (Fig. 5) some neighboring clusters have very similar colors, for clarity, we show in Fig. 12 all the learned clusters separately. It can be observed that all the clusters are well localized, even if this is not directly enforced in CDSD. In contrast, if CDSD without any constraints on W is used, the learned clusters are not localized (Fig. 15 and Fig. 16) and regions specific to ENSO are now all in a unique cluster.

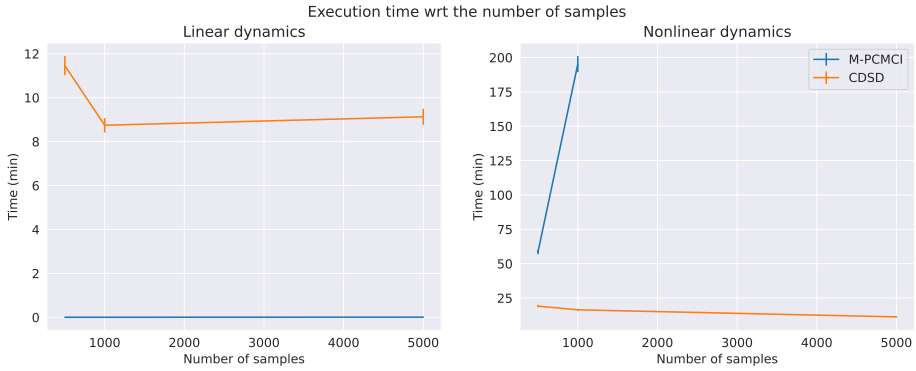


Figure 8: Comparison of the running time with respect to the number of samples in linear and nonlinear dynamics settings.

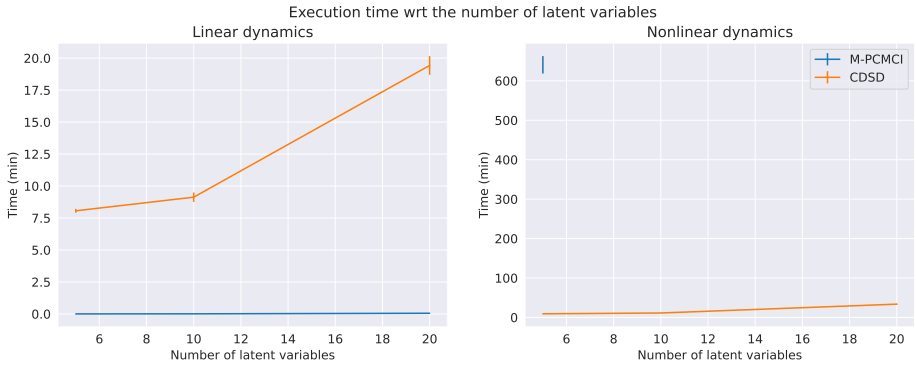


Figure 9: Comparison of the running time with respect to the number of latent variables in linear and nonlinear dynamics settings.

We also investigated using a number of latent relatively smaller ($d_z$ = 20). Fifty latents were chosen in the main text since it is close to what has been used in similar studies (60 were used in (Runge et al., 2019b)). In Fig. 13 we present the learned clustering. It can be seen that the coarser aggregation has many regions that are the union of the one observed in Fig. 5, however, interestingly, the regions related to ENSO (WPAC, CPAC, EPAC, but not ATL) are still separated. Contrary to using fifty latents, some regions are composed of disconnected regions potentially indicating that the number of latent variables is too low, see Fig. 14. For the temporal lag parameter $\tau$, we empirically observed that moderate changes did not lead to major qualitative differences. This appears consistent with the learned causal structure, where most causal effects occur at lag 1 (see in Figure 5.b)

| dynamics | density | $d_z$ | tau | t | statistics | p-value |
|---|---|---|---|---|---|---|
| linear | 0.15 | 5 | 1 | 5000 | 79 | 1.7e-03 |
| linear | 0.15 | 10 | 1 | 500 | 806 | 2.5e-03 |
| linear | 0.15 | 10 | 1 | 1000 | 590 | 5.3e-04 |
| linear | 0.15 | 10 | 1 | 5000 | 602 | 4.6e-03 |
| linear | 0.15 | 10 | 2 | 5000 | 608 | 2.4e-09 |
| linear | 0.15 | 10 | 3 | 5000 | 216 | 2.3e-12 |
| linear | 0.15 | 20 | 1 | 5000 | 1468 | 3.6e-01 |
| linear | 0.3 | 10 | 1 | 5000 | 678 | 3.6e-05 |
| nonlinear | 0.15 | 10 | 1 | 500 | 109 | 5.8e-15 |
| nonlinear | 0.15 | 10 | 1 | 1000 | 4 | 6.7e-05 |

Table 5: Wilcoxon signed-rank test statistics and p-values across experimental settings.

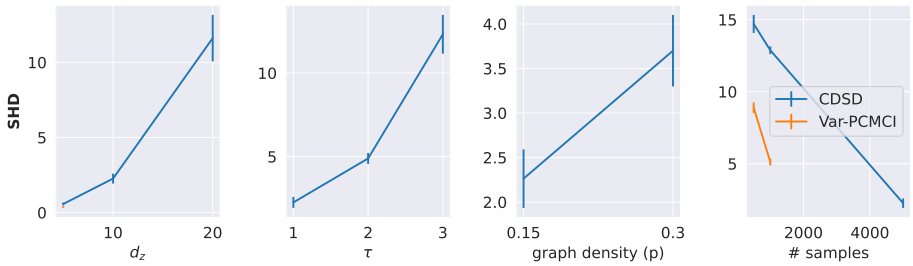


Figure 10: Comparison in terms of SHD (lower is better) on nonlinear dynamics datasets.

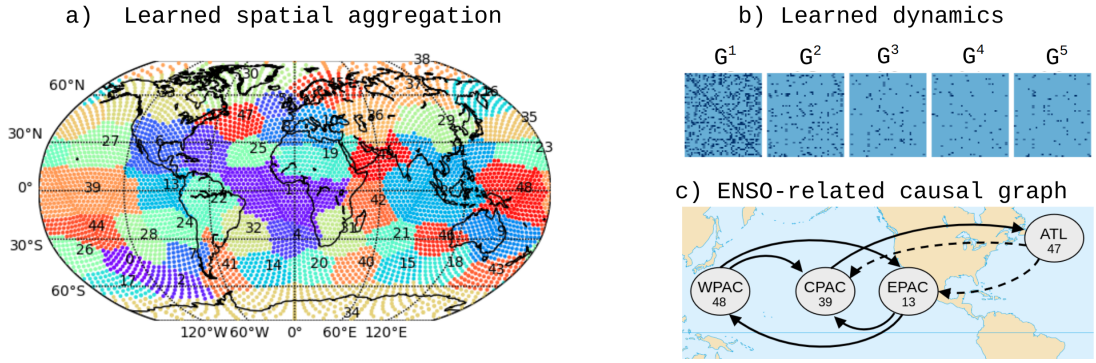


Figure 11: Spatial partitioning learned by CDSD using a lower regularisation. The dashed lines in the causal graph represent edges that were not present in the main text.

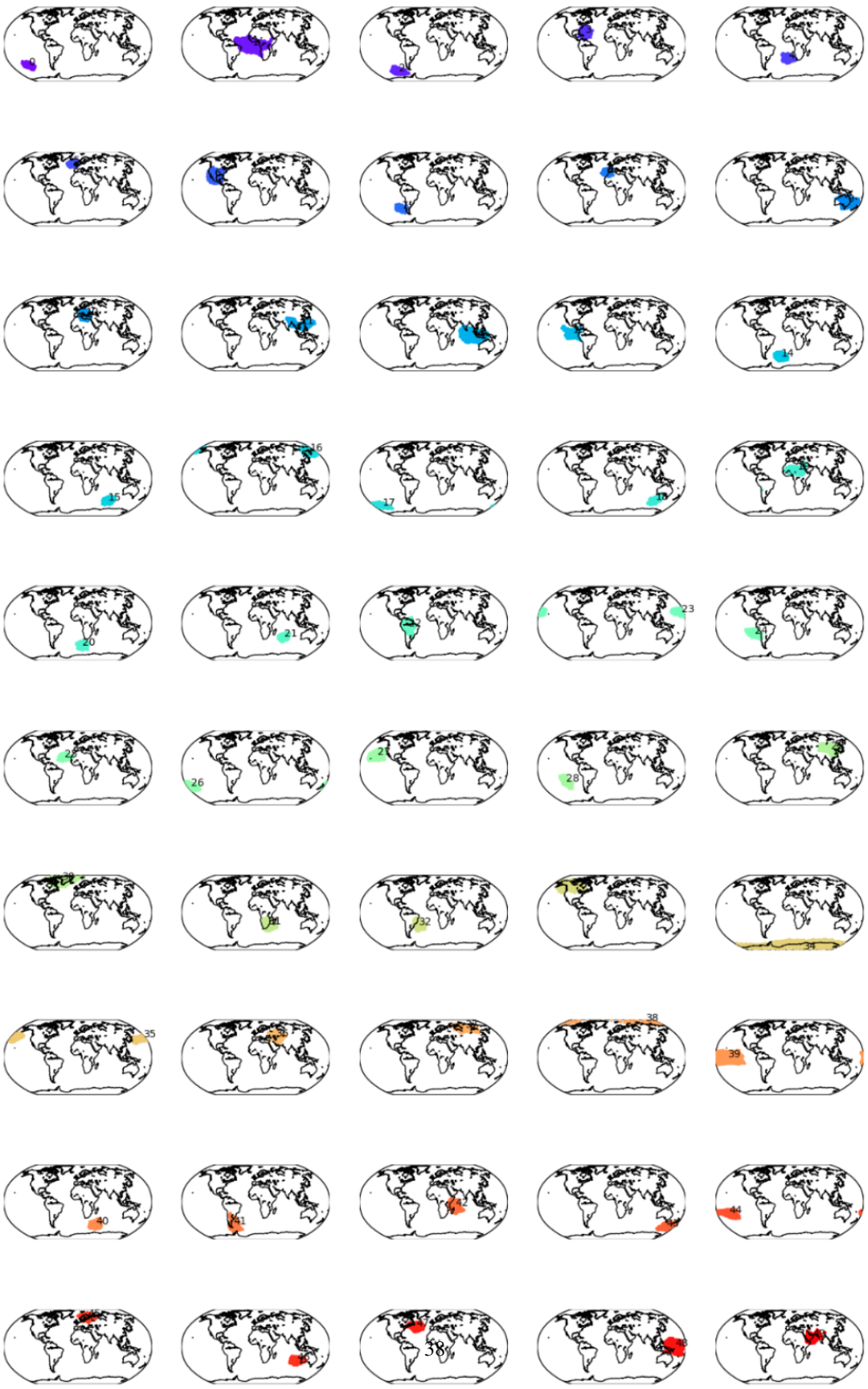

Figure 12: Representation of each region learned by CDSD.

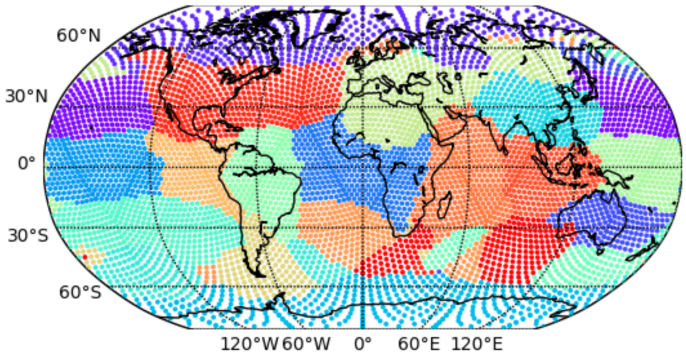


Figure 13: Spatial partitioning learned by CDSD using a low number of latents ($d_z = 20$).

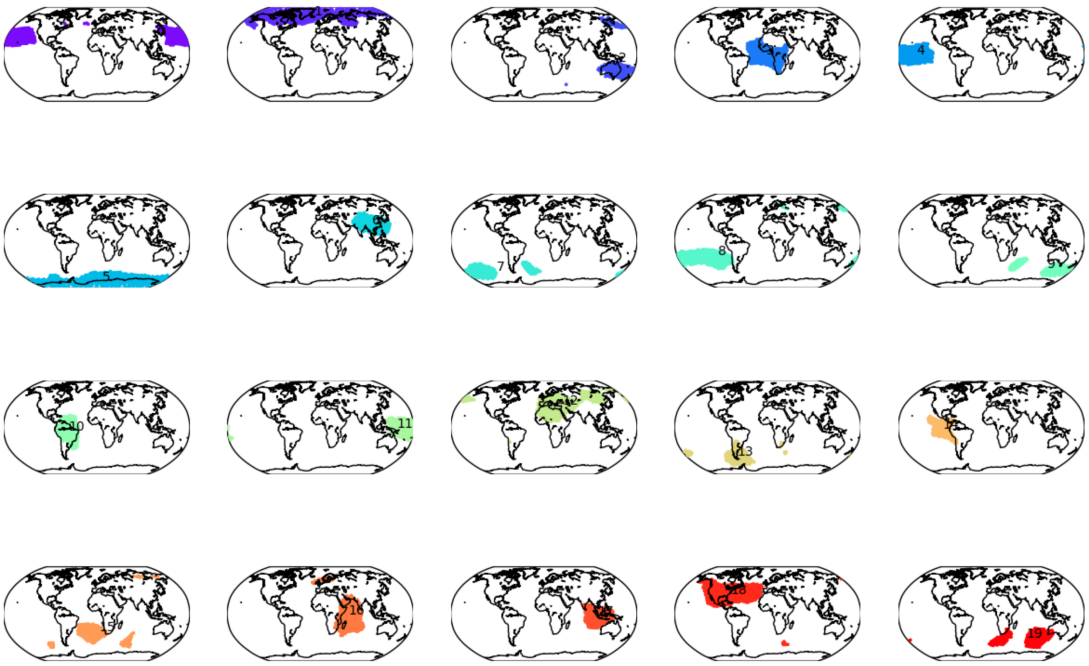

Figure 14: Representation of each region learned by CDSD using a low number of latents ($d_z = 20$).

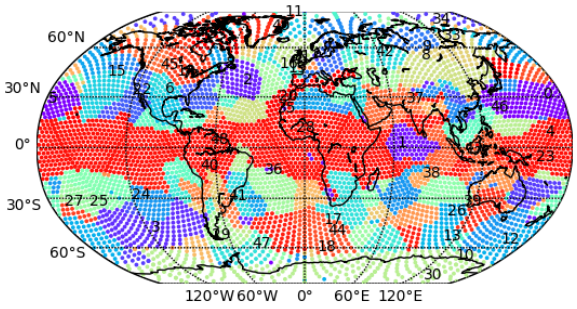


Figure 15: Spatial partitioning learned by CDSD without constraint on $W$ ($d_z = 50$).

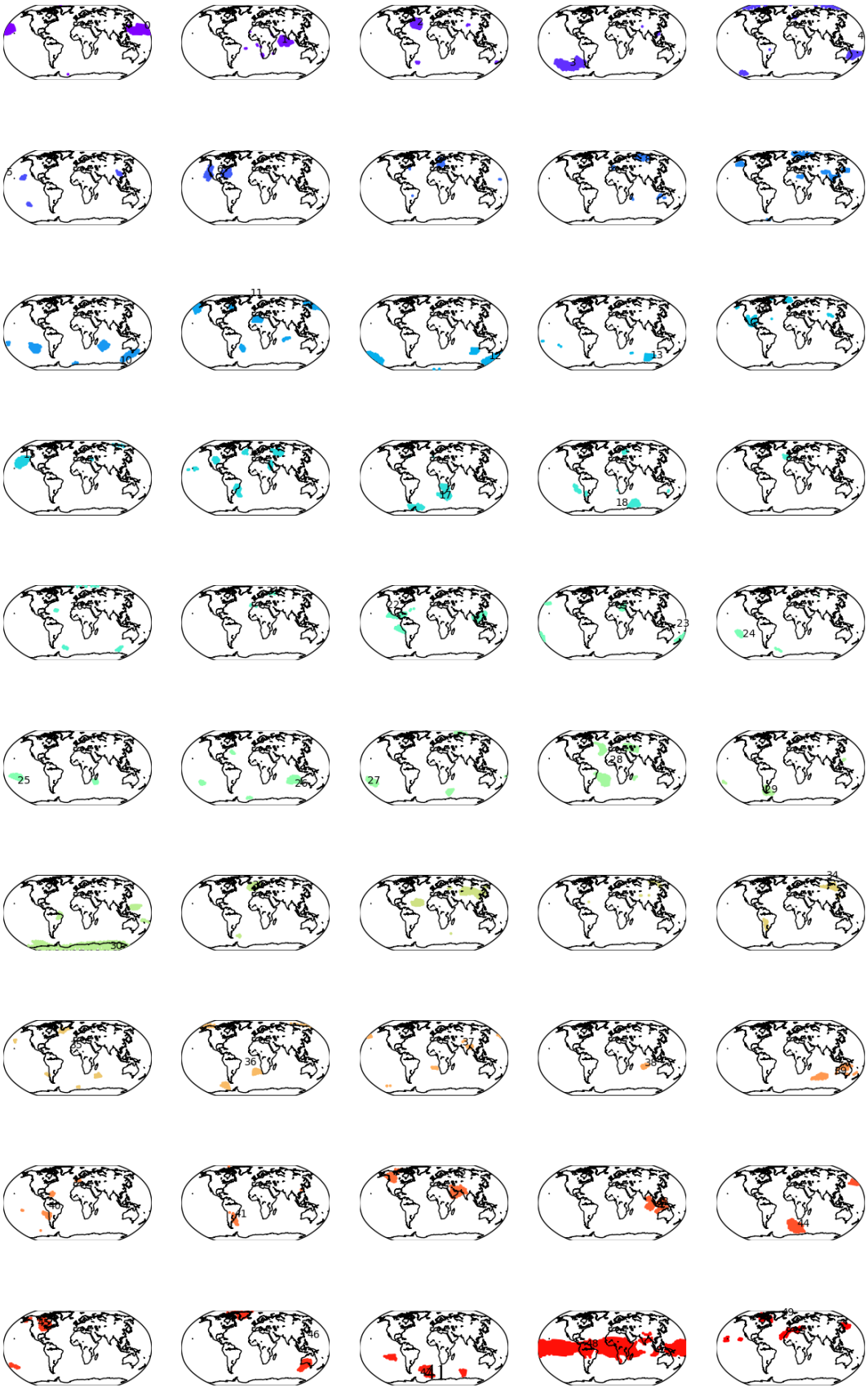

Figure 16: Representation of each region learned by CDSD without constraint on $W$ ($d_z = 50$).

## Appendix H. Extensions of CDSD

### H.1. Instantaneous Causal Relationships

In this section, we first show how to (slightly) change our objective to support instantaneous relationships. We then show a small-scale experiment we performed to validate CDSD in this setting.

In order to support instantaneous relations, we have to add two components: 1) a graph $G^0$ and the parameters $\Gamma^0$ to the generative model, and 2) an acyclicity constraint to the objective. Note that contrary to $G^1, \dots, G^\tau$, the graph $G^0$ has to be a *directed acyclic graph* (DAG) in order to have a valid factorization. We have the following modified transition model:

$$p(\boldsymbol{z}^t \mid \boldsymbol{z}^{<t}) := \prod_{j=1}^{d_z} p(z_j^t \mid \boldsymbol{z}_{\mathbf{pa}_j^{G^0}}, \boldsymbol{z}^{<t}). \tag{49}$$

Each conditional is:

$$p(z_j^t \mid \boldsymbol{z}_{\mathbf{pa}_j^{G^0}}, \boldsymbol{z}^{<t}) := h(z_j^t;\, g_j([G^0_{j:} \odot \boldsymbol{z}^t, G^1_{j:} \odot \boldsymbol{z}^{t-1}, \dots, G^\tau_{j:} \odot \boldsymbol{z}^{t-\tau}])\,). \tag{50}$$

The observation and the density models remain the same. For the objective, we add the acyclicity constraint (Zheng et al., 2018) on $\Gamma^0$:

$$\mathrm{Tr}(e^{\sigma(\Gamma^0)}) - d_z = 0. \tag{51}$$

This constraint formulation is continuous and thus differentiable. We can then use the quadratic penalty method to optimize this constrained problem (Ng et al., 2022a). The identifiability results of the latents still hold in that case. However, the identifiability of the graph $G$ is not guaranteed: at best the Markov Equivalence Class can be recovered or additional assumptions are needed such as assuming an additive noise model.

**Experimental validation.** We applied CDSD with the acyclicity constraint on 10 synthetic datasets where $G^0$ is not empty. We use the same generating process for the linear synthetic datasets of the main text (see Appendix D.1), and we make sure that $G^0$ is a DAG. As we only want a validation that CDSD can be applied in this setting, we used the default hyperparameter, skipping the hyperparameter search. We compare to Varimax-PCMCI where we set $\tau_{\min} = 0$, ensuring that PCMCI+ supports instantaneous relationships.

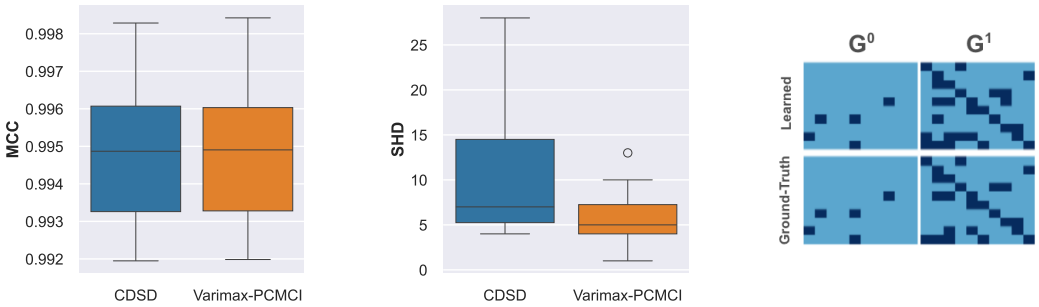


Figure 17: Validation experiments for the setting with instantaneous relations. On the left and middle, comparison of CDSD and Varimax-PCMCI in terms of MCC and SHD. On the right, comparison of the graphs learned by CDSD to the ground-truth graphs.

The results are reported in Fig. 17. We can first observe (left plot) that both CDSD and Varimax-PCMCI achieve a high MCC close to 1, as it can be expected. In terms of SHD (middle), Varimax-PCMCI is better, but CDSD is competitive, mostly considering that no hyperparameter search was performed for the sparsity regularization. We finally show a successful example (SHD $= 4$) of learned graphs by CDSD (right). For all runs, as enforced by our acyclicity constraint, we confirm that the learned $G^0$ were all acyclic.

### H.2. Using CDSD in Multivariate and Multi-Subject settings

**Multivariate case.** Researchers are often interested in multivariate problems where each feature might require different clustering. For the climate example, researchers might have several features of interest: sea-level pressure, temperature, precipitation, etc. While we only presented the univariate version of CDSD, it can easily be used as a multivariate method by slightly modifying $W$.

Assume we have $d$ features of interest. Reusing the notation from Section 3, let $\boldsymbol{x}_{ki}^t$ and $\boldsymbol{z}_{kj}^t$ be the observable and latent variables at time $t$ pertaining to the $k$-th feature. Note that now the cardinality of $d_x^k$ and $d_z^k$ can vary in function of $k$. As a matter of fact, since they are different features, it might be adequate to model them at a different coarsening. We denote the total dimensionality by $d_x := \sum_{k=1}^d d_x^k$ and $d_z := \sum_{k=1}^d d_z^k$.

For a feature $k$ we assume the observables $\boldsymbol{x}_k$ can only be related to the latent variables $\boldsymbol{z}_k$. This amounts to blacklisting some edges in $W \in \mathbb{R}^{d_z \times d_x}$. Thus, $W$ will be a block matrix of the form:

$$\begin{bmatrix} W^1 & & & \\ & W^2 & & \\ & & \ddots & \\ & & & W^k \end{bmatrix}, \tag{52}$$

where $W^k \in \mathbb{R}^{d_z^k \times d_x^k}$ is the matrix defining the connections of the variable related to the feature $k$. Besides this change, the orthogonality constraint can be directly applied to each matrix $W^k$.

**Multiple subjects case.** In many scientific applications such as neurosciences, many subjects are observed and it is often assumed that they share common properties. For example, in a brain imaging application, one could assume that the brain regions are invariant, whereas the connectivity between these regions is patient-specific (as in Monti and Hyvärinen (2018)). Similarly to the multivariate case, we can use graphs with an extra dimension ($G \in \{0,1\}^{d_p \times \tau \times d_z \times d_z}$ where $d_p$ is the number of patients) and blacklist connections along the dimension related to the patient.

### H.3. Supporting Interventions

In order to support interventions on $\boldsymbol{z}$, the model can be adapted following Brouillard et al. (2020); Gao et al. (2022); Lei et al. (2022). Assume that we have interventional data from $K$ different interventions. The $k$-th interventional distribution of the transition model $p^{(k)}(\boldsymbol{z}^t \mid \boldsymbol{z}^{<t})$ with the intervention target $\mathcal{I}_k \subseteq [d_z]$ is given by:

$$p^{(k)}(\boldsymbol{z}^t \mid \boldsymbol{z}^{<t}) := \prod_{j \in \mathcal{I}_k} p^{(k)}(z_j^t \mid \boldsymbol{z}^{<t}) \prod_{j \notin \mathcal{I}_k} p(z_j^t \mid \boldsymbol{z}^{<t}), \tag{53}$$

where $p^{(k)}$ are conditionals different from the observational conditionals except for $k = 0$ where $\mathcal{I}_0 := \emptyset$. Since there are no interventions on $\boldsymbol{x}$, the conditional $p(\boldsymbol{x}^t \mid \boldsymbol{z}^t)$ remains the same as in the

observational case. The joint interventional distribution is:

$$p^{(k)}(\boldsymbol{x}^{\leq T}, \boldsymbol{z}^{\leq T}) := \prod_{t=1}^{T} p^{(k)}(\boldsymbol{z}^t \mid \boldsymbol{z}^{<t}) p(\boldsymbol{x}^t \mid \boldsymbol{z}^t)\,. \tag{54}$$

In terms of ELBO, we now have:

$$\log p^{(k)}(\boldsymbol{x}^{\leq T}) \geq \sum_{t=1}^{T} \Big[ \mathbb{E}_{\boldsymbol{z}^t \sim q(\boldsymbol{z}^t \mid \boldsymbol{x}^t)} \left[ \log p(\boldsymbol{x}^t \mid \boldsymbol{z}^t) \right] - \tag{55}$$

$$\mathbb{E}_{\boldsymbol{z}^{<t} \sim q(\boldsymbol{z}^{<t} \mid \boldsymbol{x}^{<t})} \mathrm{KL} \left[ q(\boldsymbol{z}^t \mid \boldsymbol{x}^t) \,||\, p^{(k)}(\boldsymbol{z}^t \mid \boldsymbol{z}^{<t}) \right] \Big]. \tag{56}$$

We denote this ELBO as $\mathcal{L}_{\boldsymbol{x}}^{(k)}$. Finally, the objective changes to:

$$\begin{aligned} &\max_{W, \Gamma, \boldsymbol{\phi}} \sum_{k=0}^{K} \mathbb{E}_{G \sim \sigma(\Gamma)} \left[ \mathbb{E}_{\boldsymbol{x} \sim p^{(k)}} \left[ \mathcal{L}_{\boldsymbol{x}}^{(k)}(W, \Gamma, \boldsymbol{\phi}) \right] \right] - \lambda_s ||\sigma(\Gamma)||_1 \\ &\text{s.t. } W \text{ is orthogonal and non-negative,} \end{aligned} \tag{57}$$

where $\boldsymbol{\phi}$ is now augmented with different parameters for each conditional $p^{(k)}$.

## Appendix I. PCA-Varimax

### I.1. PCA

PCA is a commonly used dimensionality reduction method that finds a linear mapping W between the data and a latent projection having a smaller dimensionality. It can be framed as finding the projection that maximizes the variance or, alternatively, as the projection that minimizes the reconstruction loss (Pearson, 1901; Hotelling, 1933). If we consider the latter formulation, we can write the PCA method as the following optimization problem:

$$\begin{aligned} L(\boldsymbol{x}; W) &= ||\boldsymbol{x} - WW^\top \boldsymbol{x}||_2^2 \\ \hat{W} &\in \underset{W s.t. W^\top W = I_{d_z}}{\arg\min} L(\boldsymbol{x}; W), \end{aligned}$$

where $\boldsymbol{x} \in \mathbb{R}^{d_x}$ and $W \in \mathbb{R}^{d_x \times d_z}$.

In that case, the matrix W is not identifiable since any rotation would lead to the same fit of PCA (as already noted by (Anderson and Rubin, 1956)). To see this, suppose that a rotation matrix $R \in \mathbb{R}^{d_z \times d_z}$ is applied to $W$. The resulting matrix $\tilde{W} = WR$ is still orthogonal (since orthogonal matrices are closed under multiplication) and leads to the same loss since $RR^\top = I$:

$$\begin{aligned} L(\boldsymbol{x}; \tilde{W}) &= ||\boldsymbol{x} - \tilde{W}\tilde{W}^\top \boldsymbol{x}||_2^2 \\ &= ||\boldsymbol{x} - WRR^\top W^\top \boldsymbol{x}||_2^2 \\ &= ||\boldsymbol{x} - WW^\top \boldsymbol{x}||_2^2. \end{aligned}$$

### I.2. The Varimax Rotation

In practice, researchers from many different fields, such as Earth science (Vejmelka et al., 2015; Tibau et al., 2022), use a criterion called Varimax (Kaiser, 1958) in order to find a particular rotation of W. The optimal rotation according to this criterion is given by:

$$R_{\text{VAR}} = \arg\max_{R} \Big( \frac{1}{d_z} \sum_{i=1}^{d_x} \sum_{j=1}^{d_z} (WR)_{ij}^4 - \sum_{i=1}^{d_x} \Big( \frac{1}{d_z} \sum_{j=1}^{d_z} (WR)_{ij}^2 \Big)^2 \Big). \tag{58}$$

While it leads to the same loss, this rotation has been shown empirically to lead to more interpretable variables (Johnson et al., 2002; Ramsay and Silverman, 2007) (i.e., the latent dimensions are recognized as important factors of variation by experts in the fields). The criterion corresponds to maximizing the sum of the variances of the squared loadings $W_{ij}^2$. Intuitively, this criterion will make the large loadings larger and the small loadings smaller making the rotated matrix sparse. The good representation learned by PCA-Varimax when $W$ respects the single-parent assumption could be explained by the identifiability results of Zheng et al. (2022). They show that, under a more general sparsity assumption than the single-parent assumption, $W$ can be identified using an adequate sparsity regularisation.

### I.3. Empirical Validation

In this section, we show empirically that PCA-Varimax can learn a disentangled representation when the decoding function is linear and $W$ respects the single-parent assumption. The results stress the fact that PCA without the Varimax rotation generally leads to entangled representation.

The PCA-Varimax algorithm used in Varimax-PCMCI can be decomposed in three steps:

- **Step 1.** Apply PCA and recover a matrix $\hat{W}$.
- **Step 2.** Find the rotation matrix $R_{\text{VAR}}$ that maximizes the Varimax criterion. Apply this matrix to $\hat{W}$:

$$\hat{W}_{\text{VAR}} := \hat{W} R_{\text{VAR}}.$$

- **Step 3.** Apply a reflection matrix $S$:

$$\hat{W}^{+}_{\text{VAR}} := \hat{W}_{\text{VAR}} S,$$

where $S_{jj} = \text{sgn}(\arg\max_i |W_{ij}|)$ and $S_{ij} = 0$ for all $i \neq j$.

For this experiment, we do an ablation study of these three steps, namely we consider the three conditions: 1) PCA without rotation (PCA), 2) PCA with the Varimax rotation (PCA-Var), and 3) PCA with the Varimax rotation and reflection (PCA-Var+). We reuse the default synthetic datasets with the same alpha values that were chosen in the main hyperparameter search. For each condition, we present the average on 10 different datasets.

In terms of representation, it can be seen in Figure 18 that the Varimax rotation is essential to learn a disentangled representation as observed by the MCC metric. Learning a good representation has a repercussion on the recovery of the graph $G$ as shown by the SHD metric. The reflection operation might flip signs but does not have any impact in terms of disentanglement. However, if we look at the recovered matrices $\hat{W}$ in terms of absolute error with $W$, the reflection allows us to recover a matrix more similar to $W$.

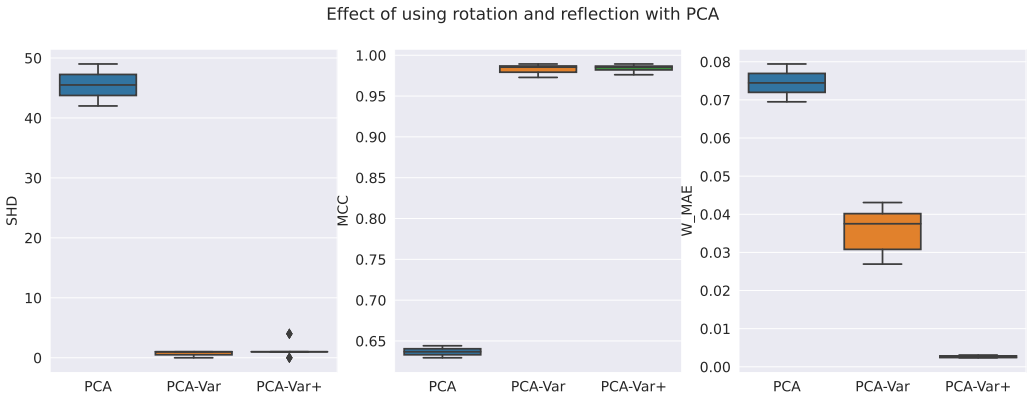


Figure 18: Comparison of 1) PCA without rotation (PCA), 2) PCA with the Varimax rotation (PCA-Var), and 3) PCA with the Varimax rotation and reflection (PCA-Var+). The Varimax rotation is crucial to recover the graph (left panel) and a good representation (middle panel). In order to recover the matrix W, the reflection operation is necessary (right panel).